Chapter 8
Wakes and Other Non-linear Effects Observed When Ultra-Short Ultra-High-Power Microwave Pulses Interact with Neutral Gas and Plasma

Y. Cao, Y. P. Bliokh, J. G. Leopold, and Ya. E. Krasik

8.1 Introduction

In this chapter we consider the physical effects, accompanying the propagation of short (less than 1 ns) powerful (several hundreds of megawatts) electromagnetic pulses of a frequency in the 10–30 GHz range in plasmas and neutral gases. Electric fields in laser pulses can be several orders of magnitude stronger than in microwave pulses, nevertheless there are phenomena which can be observed only for microwaves. These specific phenomena will be considered below.

The propagation of an electromagnetic pulse in a plasma, unbounded in the transverse direction, is defined mainly by the relation between the pulse duration, t_{pulse}, and period T_p of the electron Langmuir oscillations, $T_p = 2\pi/\omega_p$ (here $\omega_p = \sqrt{4\pi e^2 n_p/m}$ and n_p is the plasma density). The pulse is considered short if $t_{\text{pulse}} \leq T_p$.

The propagation of an electromagnetic pulse in a plasma-filled waveguide, of transversal dimensions comparable to the wavelength of the pulse, is accompanied by several specific effects absent in an unbounded plasma. For the high-power short pulse lasers considered, the dimensions of such a waveguide would be too challenging to realize at present.

A microwave pulse propagating through a neutral gas can ionize it if the pulse power density is large enough. The ionization mechanisms are different for laser and microwave pulses. For laser pulses, depending on power density and neutrals density, field ionization, multi-photon ionization and avalanche ionization are the main mechanisms. The avalanche ionization prevails in dense (atmospheric or higher

Y. Cao (✉) · Y. P. Bliokh · J. G. Leopold · Ya. E. Krasik
Department of Physics, Technion-Israel Institute of Technology, 320000 Haifa, Israel
e-mail: yangcao@campus.technion.ac.il

T. Shao and C. Zhang (eds.), *Pulsed Discharge Plasmas*,
Springer Series in Plasma Science and Technology,
https://doi.org/10.1007/978-981-99-1141-7_8

pressures) gases. The electron-neutral collision frequency in gases of low density is small, so the pulse has no time to produce plasma of significant density.

Avalanche ionization is the main mechanism of neutral gas ionization by a powerful microwave pulse. If the gas pressure is of the order of 10^2–10^3 Pa, during the pulse ($t_{pulse} \sim 1$ ns), the density of the newly created plasma can reach the critical value, for which the microwaves cannot penetrate the plasma. It seems reasonable to expect that the interplay between the pulse characteristics and time-varying parameters of the plasma is much stronger for microwave than for laser pulses. However, HPM sources with peak power >1 GW and sub-ns pulse duration became available only recently [1, 2].

Theoretical and experimental investigation of short powerful microwave pulses propagating in neutral gases, plasma and plasma-filled waveguides were performed at the Technion during last few years. Results of these investigations have been published in Refs. [3–13], some of which will also be described below. Two sub-nanosecond microwave sources at ~10 and ~30 GHz and two different waveguides were used. Theoretical and experimental results are in good not only qualitative, but in quantitative agreement as well.

8.2 Ionization-Induced Phenomena in Neutral Gases and Plasmas

8.2.1 Experimental Setup

There are several different high-power microwave (HPM) sources capable of producing peak power up to several GW with duration <100 ns [14]. However, for the microwave energy of tens and hundreds J, the required high-voltage drivers are large (>10 m). For short microwave pulse duration ($\leq$1 ns), the most suitable and compact HPM source is a super-radiant backward wave oscillator (SR-BWO), which can generate pulses of peak power from hundreds of MW to a few GW [1, 2, 15–17].

The experimental system [10] designed to investigate the effect of a focused HPM pulse (9.6 GHz, 500 MW, 0.5 ns) on a neutral gas and plasma filling a Pyrex tube, is shown in Fig. 8.1.

The slow-wave structure (SWS) of the SR-BWO was driven by a high current hollow electron beam (1.6 kA, 300 keV, 5 ns) generated in a magnetically insulated diode by a hollow carbon cathode with a sharp circular edge. The diode was supplied by a high voltage pulse produced by an all-solid-state generator based on magnetic compression stages and semiconductor opening switches. The electron beam was guided through the SWS by a pulsed magnetic field (3 T, 10 ms). At the exit of the SWS, the microwave mode is converted from TM_{01} mode to TE_{11} mode using a specially designed mode converter. The latter radiates through a circular cross section horn antenna in the form of a linearly polarized Gaussian beam. The microwave beam had a width of ~5 cm Full Width at Half Maximum (FWHM) at ~10 cm

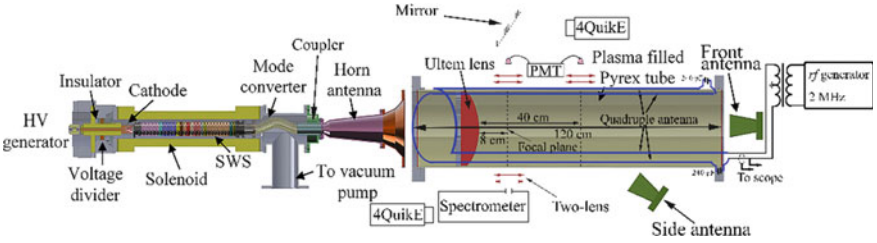

Fig. 8.1 Schematic drawing of the experimental setup to for studying the HPM (9.6 GHz, 500 MW, 0.5 ns) pulse interaction with neutral gas and plasma, including the HPM source, emitting horn, Ultem lens, and the interaction tube made of Pyrex. Various diagnostic probes are also pointed out. Note, a quadruple antenna attached to the Pyrex tube wall, and powered by a 2 MHz, 5 kW rf generator [10]

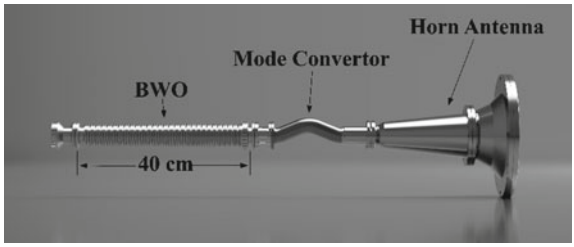

Fig. 8.2 Appearance of the SR-BWO, mode converter, and horn antenna wave structure

downstream from the antenna output aperture (at the inner surface of the Perspex interface insulator window of the experimental tube). A picture of the SR-BWO, mode converter, and antenna is seen in Fig. 8.2. The background pressure (~6 mPa) in the magnetically insulated diode, slow-wave-structure, mode converter, and horn antenna was maintained by a turbo-molecular pump.

The waveform of the microwave electric field, measured at 120 cm from the horn antenna, and the calculated microwave instantaneous and averaged power over a period are shown in Fig. 8.3. The maximum electric field amplitude reaches ~12 kV/cm and the total power of the ~0.5 ns long HPM pulse, reaches 550 MW. The central frequency of the microwaves was found to be 9.6 GHz. The pattern of the HPM pulse obtained on a board with a matrix of neon micro-lamps (see Fig. 8.3c) confirms the TE_{11} mode of the radiation.

In experiments [7, 9] studying the interaction of the HPM pulse and neutral gas and plasma, a hyperbolic Ultem lens was inserted inside an 80 cm long Pyrex tube with an inner diameter of 24 cm (see Fig. 8.1). This dielectric lens focuses the HPM pulse on a focal plane located 9 cm from its tip. For full power of the microwave beam, the radial distribution of the beam intensity near the focal region was not measured because of electrical breakdown inside the receiving antenna. Instead, using a network analyzer, low power 9.6 GHz TE_{11} microwaves were fed into the horn antenna and the radial distribution of the microwave power inside the Pyrex tube was measured by moving the receiving antenna along the tube radius and axis [7].

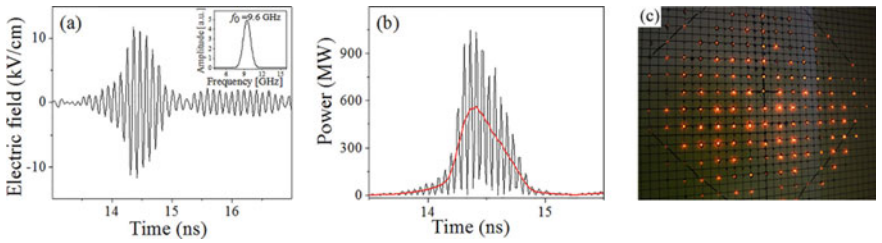

Fig. 8.3 **a** Waveform of the measured electric field at a distance of 120 cm from the horn antenna; inset: FFT of the microwave signal; **b** calculated total microwave instantaneous power and averaged power over period, where time is relative to the time when the electron beam is collected on the wall of the SR-BWO; **c** HPM pulse pattern obtained at a distance of 0.5 m from the horn antenna on the neon micro-lamps matrix [4]

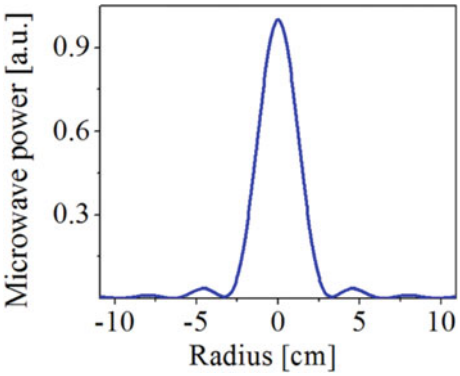

Fig. 8.4 MAGIC simulated radial distribution of the microwave power in vacuum on the focal plane [7]

Results of these measurements showed good agreement with MAGIC simulations [18]. These simulations for 9.6 GHz (see Fig. 8.4), confirmed that at the focal plane, the beam has a Gaussian profile, $P(r, t) \propto \exp\left(-t^2/t_b^2\right)\left(-r^2/r_b^2\right)$, where $t_b = 0.37$ ns (0.6 ns at FWHM) and $r_b = 1.6$ cm and that the electric field maximum is 150 kV/cm for 500 MW microwave input power. The Rayleigh length of the HPM pulse is ~5.4 cm.

To fill the Pyrex tube by plasma we used radio frequency (rf) discharge sources attached to the walls of the tube. The parameters of the plasma, generated in either neutral Ar or He were characterized using different methods. A detailed description of the plasma generation and characterization can be found in Refs. [5, 8]. The plasma was generated at a pressure in the range 5–130 Pa using a 2 MHz rf generator with a matching system and a quadruple antenna (see Fig. 8.1). Good matching was obtained between the plasma parameters, measured by a movable Langmuir probe, microwave cut-off, interferometry, and optical emission spectroscopy. The plasma parameters such as the density and temperature can be adjusted by controlling the rf power on the quadruple antenna and the gas pressure, in the range 1×10^{10}–5×10^{12} cm^{-3} and 1–3.5 eV respectively. In the absence of the dielectric lens, the

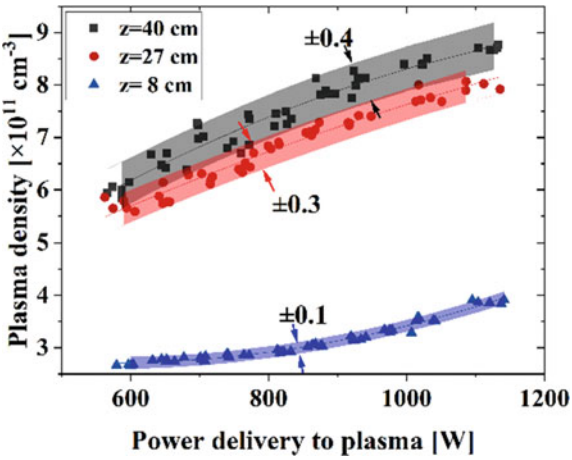

Fig. 8.5 Average plasma density versus the rf power measured at different axial distances from the tip of the Ultem lens at z = 0 for 50 Pa neutral He [8]

axial and radial distributions of the plasma density was found to be uniform in along ~60 cm axially and ~10 cm radially. The presence of the lens introduces changes in these distributions near the lens surface because of the influence of the dielectric material on the rf field configuration and absorption/desorption processes. Radially averaged densities measured by microwave interferometry, increase gradually along the axis when the lens is present (see Fig. 8.5).

A standard WR90 antenna, installed at the output of the Pyrex tube, with 10 dB gain was used to measure the output HPM's radial distribution and the waveform of the transmitted radiation. The waveform is registered by an Agilent oscilloscope (12 GHz, DSO81024B). The transverse power distribution of the microwave radiation at various longitudinal positions inside the Pyrex tube was observed by an array of 400 miniature Ne lamps, 4 mm diameter each. Microwave measurements were performed inside an anechoic room (2 m × 1.2 m × 1.8 m) covered by absorbing material (17 dB at 10 GHz). This well instrumented experimental setup has been designed for the detection and study of ionization-induced phenomena, described below, which accompany the HPM pulse propagation in neutral gases and plasmas.

8.2.2 Ionization-Induced Self-channeling. Theoretical Analysis

A powerful electromagnetic (EM) wave propagating through a medium can change the medium properties, which in turn, affects the wave characteristics. Thus, this process is to be treated as a self-consistent nonlinear problem. There are many phenomena which accompany propagation of an arbitrary wave through a medium the response of which is nonlinear. These are solitary waves (solitons), modulation

instability of wave packets, wake excitation by the EM pulse moving in plasma, self-channeling of a wave beam, high harmonics generation, etc.

For EM waves, plasma is the most suitable medium where many of the phenomena listed above manifest themselves most clearly, and self-channeling of the EM beam is one them. Various mechanisms can be responsible for self-channeling [19–23]. The guiding profile of the refractive index (with minimum on the beam axis) appears as a result of the interaction of the plasma with the beam.

The character of the EM pulse interaction with plasma depends on a value of the *strength parameter* a_0 which is defined as

$$a_0 = \left(\frac{2e^2\lambda^2 I_0}{\pi m^2 c^5}\right)^{\frac{1}{2}} \simeq 6.7 \cdot 10^{-6}\frac{\lambda}{r_0}\sqrt{P_0[W]}. \tag{8.2.1}$$

here λ is the wavelength, I_0 and P_0 are the wave's peak intensity and power, respectively, and r_0 is the beam radius. It is assumed that the radial profile of the wave amplitude is Gaussian, i.e., $a(r) = a_0\exp\left(-r^2/2r_0^2\right)$. The parameter a_0 defines the amplitude of the electron oscillatory velocity, $v_\sim$, in the field of the EM wave: $v_\sim = ca_0$. The ponderomotive force $\boldsymbol{F}_p$ is also defined by this parameter:

$$\mathrm{F}_p = -\frac{mc^2\nabla\left(a^2\right)}{2}. \tag{8.2.2}$$

Propagation of the EM pulse through neutral gas at pressure $\sim 10^3$ Pa was studied using the pulse of $P \cong 300$–500 MW power and $f = 9.6$ GHz frequency. A dielectric lens formed the Gaussian beam of ~ 3 cm diameter waist. Thus, the strength parameter at waist is $a_0 \cong 0.2$. The amplitude of the wave's electric field component, $E_0 \cong 3.2 \cdot 10^6 a_0/\lambda \cong 160 - 200$ kV/cm, is sufficient for initiating an intense avalanching process and consequently, plasma formation. Thus, at least part of the pulse propagates in the resulting plasma. It is important to note here that the ponderomotive force, which plays a crucial role in the self-channeling of an intense laser beam [19] propagating through plasma, cannot be responsible for self-guiding of microwave beams for the above parameters. The reason for this is because the ponderomotive force Eq. (8.2.2) requires considerably longer time [several nanoseconds compared to the pulse duration (<1 ns)] to be able to move electrons to a distance comparable to the beam radius and therefore it cannot be responsible for the redistribution of the plasma density to form a channel.

However, the ionization process itself can produce the guiding profile of the plasma density. This can occur when the energy of electrons, oscillating in the microwave field, is large enough, and the cross section σ_i of the electron impact ionization process is a *decreasing* function of the energy resulting in higher ionization rate at the beam periphery than on the beam axis. This leads to the formation of plasma with a focusing radial profile (the refraction index having minimum on axis). This ionization-induced self-channeling of a microwave pulse was predicted in [24, 25] and discovered experimentally in Refs. [7, 9].

Microwave Pulse Self-channeling in a Neutral Gas

Let us consider a model of the plasma formation due to neutral gas ionization by a powerful microwave beam. The time evolution of the electron density, $n_e(r, t)$, is described by

$$n_e(r,t) = n_0 \exp\left\{ n_g \int_{-\infty}^{t} dt' \sigma_i \left[w\left(r,t'\right) \right] \left| v\left(r,t'\right) \right| \right\}. \tag{8.2.3}$$

Here n_0 and n_g are the initial electron and neutral gas densities, respectively, v is the electron velocity and $w = mv^2/2$ is the electron energy. It is convenient to use the quantity $\mathcal{E} = 10^{-5}E$ [V/cm] as a scaled value of the electric field ($\mathcal{E} = 1$ if $E = 10^5$ V/cm). Then, w [eV] $= 10^4$ $(\mathcal{E}\ \lambda/2\pi)^2$ $\cos^2\omega t$, and $v = 0.1c$ $(\mathcal{E}\ \lambda/\pi)$ $\cos\omega t$, where $\omega = 2\pi f$.

For a Gaussian microwave beam of maximum amplitude $\mathcal{E}_{00}$, the dependence of the amplitude of the electric field on r and t is given as

$$\mathcal{E} = \mathcal{E}_0(r) e^{-t^2/2t_{pulse}^2},\ \mathcal{E}_0(r) = \mathcal{E}_{00} e^{-r/2r_0^2}.$$

If $\omega t_{\text{pulse}} \gg 1$, it is convenient to use quantities averaged over the period of the field oscillation and present the integral in Eq. (8.2.3) as follows (see Ref. [7] for details):

$$\int_{-\infty}^{t} dt' \sigma_i |v| \cong \frac{10^{-17} c t_{pulse}}{\pi F(\theta; b)}. \tag{8.2.4}$$

Here $\theta = t/t_{\text{pulse}}$, $b = \mathcal{E}_0\ (r)\lambda$, and the function F is defined as

$$F(\theta; b) = \int_{-\infty}^{\theta} d\theta' e^{-\frac{\theta'^2}{2}} \frac{1}{2\pi} \int_{-\pi}^{\pi} d\tau |\cos\tau| \sigma_i \left\{ \frac{10^4}{4\pi^2} [\mathcal{E}_0(r)\lambda]^2 e^{-\theta'^2} \cos^2\tau \right\}. \tag{8.2.5}$$

Here σ_i is the ionization cross section measured in units of 10^{-16} cm^2. The dependence of $F(\theta; b)$ on θ for various values of the parameter b is shown in Fig. 8.6 for He.

The function $F(\theta; b)$, shows monotonic increase for b < 4 so that the plasma has maximal density and electric field on the beam axis and both decrease towards its periphery. However, when the field intensity is large enough, i.e., $b > 4$, the behavior is different. During the second half of the pulse the function $F(\theta; b)$ decreases as the electric field increase (see $b = 9$ in Fig. 8.6). This indicates that during the first half of the pulse, the density of plasma is maximal axis. During the second half of the pulse, the plasma density on axis is smaller than at the beam periphery. The plasma density reaches its maximal value at a certain radius where it forms a plasma channel with plasma density decreasing towards the axis. For a plasma channel to form in both He and air for $b \geq 4$, the electric field should be ≥130 kV/cm. Above this threshold, the

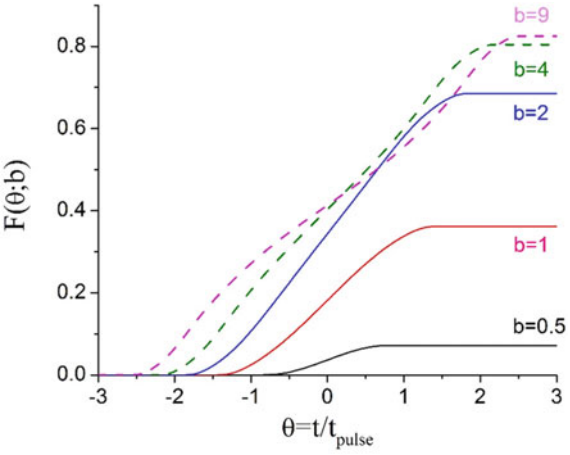

Fig. 8.6 The dependence of the function $F(\theta; b)$ on θ for various values of the parameter b in He using σ_i from Ref. [26]. Here $\theta = 0$ corresponds to the temporal center of the pulse

plasma density is independent of electric field after the pulse propagation ($\theta \approx 2$), resulting in the value $F(\theta; b) \approx 0.8$ for He. The plasma density after the pulse can be estimated as

$$\ln\left(\frac{n_{\text{final}}}{n_0}\right) \cong A p t_{\text{pulse}} \tag{8.2.6}$$

Here $p(Torr)$ is the gas pressure, $t_{\text{pulse}}(ns)$ is the pulse duration, and A is a coefficient equal to 2.8 and 20 for He and air, respectively. An example of the plasma density evolution in time and space for He and field amplitude $b = 5$ ($E \approx 150$ kV/cm) is shown in Fig. 8.7. One can see that the maximum density of the plasma is at radius $r \approx r_0$ at the normalized time $\theta \approx 1.2$. The microwave beam can propagate through this plasma with a guiding profile (plasma channel) if the density on axis is under critical, n_{crit}, defined by $4\pi e^2 n_{\text{crit}}/m = \omega^2$. Thus, assuming an electric field amplitude $E \approx 150$ kV/cm, and $n_0 \approx 10^5$ cm^{-3}, then for $t_{\text{pulse}} = 0.37$ ns self-channeling occurs at $4 \cdot 10^3$ Pa pressure in He and at $6 \cdot 10^2$ Pa in air.

To support this model, a numerical study of the plasma formation was carried out using a one-dimensional (1D) PIC Monte Carlo collisional simulation code (a detailed description of this code is presented in Ref. [27]). The code considers the momentum transfer of electron-neutral collisions, electronic levels excitation of neutrals, and the ionization processes. In these simulations, the electromagnetic pulse parameters were: peak electric field, $E = 150$ kV/cm, pulse duration, $t_{\text{pulse}} = 0.37$ ns and $r_0 = 1.6$ cm. A seed electron density of 10^5 cm^{-3} triggers the electron impact ionization of air or helium. The results of these simulations show that at the peak of the pulse in He at $p = 4.5 \cdot 10^3$ Pa, the plasma density reaches $n_e \approx 2.3 \cdot 10^{12}$ cm^{-3} at $r = 2$ cm and $n_e \approx 6 \cdot 10^{11}$ cm^{-3} at $r = 0$. Plasma with such density profile, allows the microwave beam to propagate through the central plasma channel while at the beam periphery it is reflected by the over-critical plasma. Similar results were obtained for air at a pressure of 10^3 Pa. For higher gas pressures, the microwave

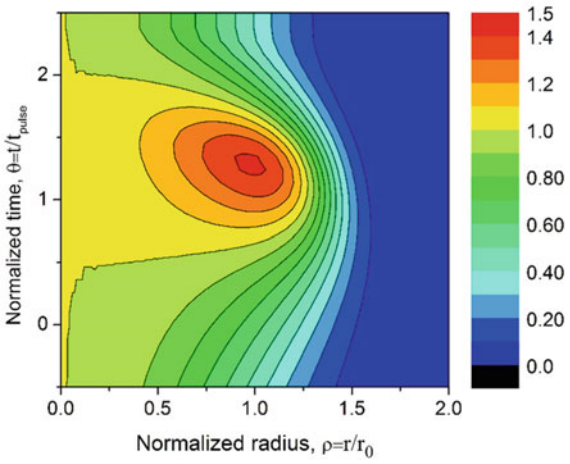

Fig. 8.7 Contour plot of the plasma density (in He) versus the microwave beam normalized radius and time, for $b = \epsilon_0(r)\lambda = 5$. The density is normalized by its value $n_e(0, t)$ on the beam axis. Normalized time $\theta = 0$ corresponds to the temporal center of the pulse

is reflected and scattered before such channel forms due to the fast plasma density growth to over-critical density. The channeling will not occur when the electric field smaller than 150 kV/cm.

Microwave Pulse Self-channeling in a Preliminarily Formed Low-Density Plasma

The results presented in section "Microwave Pulse Self-channeling in a Neutral Gas" demonstrate that at some certain conditions one can obtain he formation of a plasma with density less in the center than at the periphery (see Fig. 8.6 and explanations below) leading to the EM pulse capture. This density profile is formed at the rear part of the pulse and the main part of the pulse is not captured into the plasma channel. It seems reasonable to create a low-density plasma preliminarily with minimal density on the pulse axis. In the experiments [8], this plasma was generated inside the tube filled with the neutral gas by a 2 MHz inductively coupled discharge, induced by a quadruple antenna.

In the experiments, the EM pulse is injected into the tube through an Ultem lens. In the absence of the lens, the axial and radial distributions of the plasma density is close to uniform [6]. The lens changes considerably the initial plasma density distribution $n_{pl}(r, t = 0)$ because of plasma ions recombination, absorption, neutral desorption, etc., occurring at the lens surface. These processes and the convexity of the lens surface leads to an initial plasma density smaller along the axis. This is a favorable initial condition for the self-channeling of the microwave pulse even for smaller neutral density or lower pulse power.

Let us model the radial distribution of the initial plasma density $n_{pl}(r, t = 0)$ on the focal plane as

$$n_{pl}(r, t = 0) = n_0\left(1 - \Delta n e^{-\frac{r^2}{\Delta r^2}}\right). \tag{8.2.7}$$

where the parameters Δn and Δr characterize the depth and the width of the density dip near the axis. To estimate the range of the plasma and microwave parameter values that allow self-channeling, let us assume a step like radial plasma density distribution across the channel instead of it being smooth. Namely, let us associate the plasma density $n_1 = n_e(0, t)$ at the axis (local minimum density) with the entire channel core plasma density, and the density n_2, $n_2 > n_1$, of the local maximum (if it exists) at the microwave beam periphery, as the channel wall plasma density. Such a "hollow" plasma channel can trap a microwave beam, just like an optical fiber when the difference between the reflection coefficients of the channel core and wall becomes sufficient for total internal reflection (TIR) of the focused microwave beam. The angle of divergence of the Gaussian beam, φ_{beam}, can be estimated as $\varphi_{\text{beam}}[rad] \cong \lambda/\pi r_0$, where λ is the microwave wavelength, and r_0 is the beam waist radius at the focal plane. The beam will be trapped in the channel when the angle of incidence α at the interface between the channel core and the wall exceeds the critical value α_{TIR}, defined as

$$\sin^2\alpha_{\text{TIR}} = \frac{1-\frac{n_2}{n_1}}{1-\frac{n_1}{n_{\text{crit}}}}. \tag{8.2.8}$$

Using the beam parameter values $\lambda \approx 3$ cm and $r_0 \approx 2 - 3$ cm, φ_{beam} can be estimated to be $\varphi_{\text{beam}} \approx 0.32$ (the value $r_0 \approx 3$ cm will be used hereafter for definiteness). The angle of divergence φ_{beam} and the angle of incidence are related as $\varphi_{\text{beam}} + \alpha = \pi/2$, so that the TIR condition $\alpha \geq \alpha_{TIR}$ can be written as

$$\sin^2\varphi_{\text{beam}} \leq \frac{n_2-n_1}{n_{\text{crit}}-n_1}, \tag{8.2.9}$$

or

$$\Phi(t) \equiv \frac{\sin^2\varphi_{\text{beam}}}{\frac{n_2(t)}{n_1(t)}+\sin^2\varphi_{\text{beam}}-1} \leq \eta(t) \equiv \frac{n_1(t)}{n_{\text{crit}}} \leq 1. \tag{8.2.10}$$

The inequalities (8.2.10) define the time interval in which self-channeling can occur. The evolution of the plasma density $n_e(r, t)$ is described by Eq. (8.2.3) by substituting n_0 with $n_{pl}(r)$ from Eq. (8.2.7). The functions $\Phi(t)$ and $\eta(t)$ are defined by the solution of this equation. Figure 8.8 demonstrates when, relative to the pulse center, conditions (8.2.10) are satisfied in a homogeneous (Fig. 8.8a) and radially inhomogeneous (Fig. 8.8b) initial plasma. For inhomogeneous plasma density we used $\delta n = 0.3$, $\Delta r = 1.3r_0$, neutral gas pressure $p = 260$ Pa, maximal amplitude of the electric field pulse $E_0 = 200$ kV/cm, and initial plasma density $n_0 = 0.17n_{\text{crit}}$. Moderate deviations from these parameters leads to qualitatively similar results. For a homogenous plasma, one can see in Fig. 8.8a that self-channeling can occur only near the end of the pulse. On the other hand, a significant initial plasma inhomogeneity (see Fig. 8.8b) affects the part of the pulse which can be trapped into the channel.

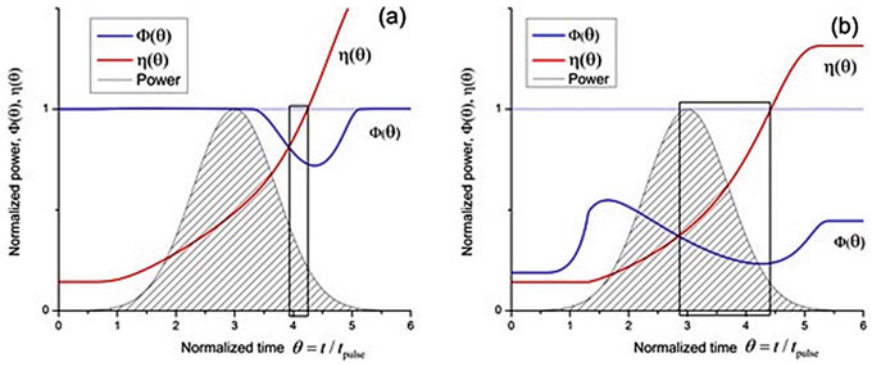

Fig. 8.8 Graphical representation of the inequalities Eq. (8.2.10). **a** Radially homogeneous distribution of the initial plasma density. **b** Inhomogeneous plasma density. The functions $\Phi(\theta)$ and $\eta(\theta)$ are obtained as solutions of Eq. (8.2.3). The normalized microwave pulse intensity is shown by the shaded area. The microwave beam is trapped in the hollow plasma channel when $\Phi(\theta) \leq \eta(\theta) \leq 1$ (regions, marked by rectangles). Normalized time $\theta = 0$ corresponds to the temporal center of the pulse

The propagation of the pulse through neutral gas in the presence of a radially inhomogeneous initial plasma component can be described qualitative as follows. Let the initial plasma density n_0 be small compared to the critical density, $n_0 \ll n_{crit}$. At the beginning of the pulse, the ionization rate is maximal at the axis. The plasma density grows due to neutral gas ionization and becomes maximal near the axis and its value can be comparable with the critical one. This radial distribution of the plasma density acts as a defocusing medium and scatters part of the electromagnetic wave energy in the radial direction. Later, when the electric field of the pulse is strong enough, the ionization rate maximum is shifted to the wave beam periphery. Gradually, the plasma density maximum is shifted from the axis and approaches its critical density. Then, instead of scattering, the plasma traps the wave into the channel. The scattered waves disappear, while the EM energy which propagates along the axis increases. Experimentally, this scenario can be observed using two receiving antennas. One antenna is to be placed along the axis far downstream from the focal plane of the lens (receiving antenna in Fig. 8.1) and a second antenna placed at an angle from the axis to receive the scattered signal from the focal region (side antenna in Fig. 8.1). The receiving antenna should register a two-humped pulse, while the side antenna should have one maximum. The minimum of the receiving antenna signal is to be associated with the wave's scattering, which is responsible for the signal received by the side antenna.

8.2.3 *Experiments on the Interaction of Powerful Microwave Pulses with Neutral Gases and Plasmas*

Interaction with a Neutral Gas

A detailed description of the results of these experiments are presented in Refs. [7, 9]. Wide field view patterns (72 cm) of the plasma light emission, taken with a digital camera (Nikon D300S), operated with open shutter displaying the time-integrated light emission of the plasma generated by the HPM pulse are shown in Fig. 8.9 for different pressures in the range $6 \times 10^2 < p < 3 \times 10^3$ Pa in air and $3 \times 10^3 < p < 1.5 \times 10^4$ Pa in He. One can see for 5×10^3 Pa helium, the plasma channel is with length of ~40 cm and diameter of ~4 cm, ~7 times longer than the Rayleigh length. This is a direct evidence of plasma-induced self-channeling of the HPM pulse. At other pressures of He or in air, such long channels were not obtained showing that self-channeling could be realized only in narrow range of pressures for given power of the HPM pulse.

Front view of the beginning of the plasma light emission take by a fast framing camera focused on the focal plane are shown in Fig. 8.10 for air and He at various pressures. One can see within a ~ 4 cm diameter area, approximately uniform distribution of the plasma light emission for $p = 1.5 \times 10^4$ Pa in air (Fig. 8.10b) and for $p = 3 \times 10^4$ Pa in He (Fig. 8.10d). However, for $p = 10^3$ Pa in air and $p = 4.5 \times 10^3$ Pa in He, a hollow central region is seen (see Fig. 8.10a, c, respectively). These values agree with the results of the model in section "Microwave Pulse Self-channeling in a Preliminarily Formed Low-Density Plasma". A sequence of frames distributed in time show that this hollow structure light intensity appears during ~1 ns and then it fills in. This indicates that a hollow cylindrical plasma with reduced density around the axis develops at focus during the time interval when the HPM pulse crosses this plane.

The power distribution of the transmitted microwave beam at a distance of 10 cm downstream from the focal plane was observed by a Ne lamps matrix (see Fig. 8.11). The microwave pattern's diameter was ~9 cm at vacuum and atmospheric pressure air (Fig. 8.11a, d), which agrees with the Gaussian beam expansion at this position obtained by MAGIC simulations. When the Pyrex tube was filled with gas, with pressure within $3 \times 10^3 < p < 6 \times 10^3$ Pa for He and $5 \times 10^2 < p < 10^3$ Pa for

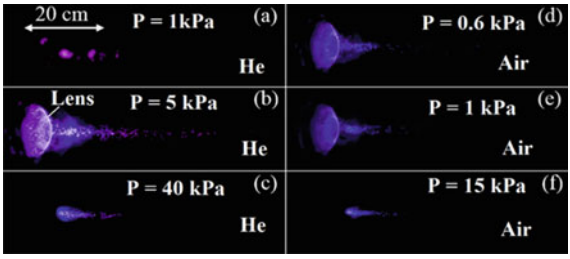

Fig. 8.9 Time-integrated side view of the light emission from the plasma for He: **a** 10^3 Pa, **b** 5×10^3 Pa, **c** 4×10^4 Pa; and air: **d** 6×10^2 Pa, **e** 10^3 Pa, and **f** 1.5×10^4 Pa [7]

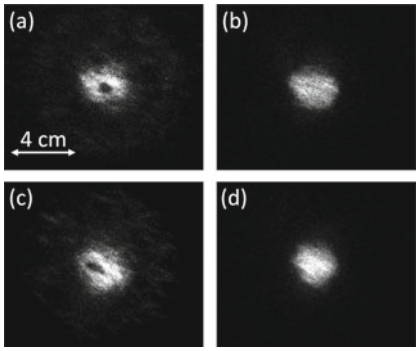

Fig. 8.10 Fast-framing images (1.2 ns exposure time) of the plasma light emission obtained in air with pressure of **a** 10^3 Pa; **b** 1.5×10^4 Pa, and helium **c** 4.5×10^3 Pa; **d** 3×10^4 Pa [7]

air, the pattern diameter decreased to ~4–5 cm (Fig. 8.11b, e), suggesting that only the central part of the beam propagates. For higher gas pressure ($10^3 < p < 10^4$ Pa for He and $6 \times 10^3 < p < 2 \times 10^4$ Pa for air) the radius and intensity of light emitted by the Ne lamps in the central part of the pattern reduce, indicating on a dense plasma formation at that location. These observations (see Fig. 8.11b, e) agree with the data obtained with front view images for the same pressure range, showing a hollow structure of the plasma light emission pattern (see Fig. 8.10a, c) indicating on formation of the plasma channel with significantly lower density close to the axis than at the HPM pulse periphery. At even higher pressures, the central part of the HPM pulse is blocked by the plasma and only the periphery of the beam is reflected on the Ne lamps screen (see Fig. 8.11e, f).

Prefilling of the Pyrex tube by either He or air, changes the transmitted power and the temporal profile of the HPM pulse because of plasma formation due to pulse induced gas ionization. The dependence of the peak microwave power normalized to its maximum value in vacuum measured by the receiving antenna at the distance $z = 120$ cm from the tip of the Ultem lens as a function of the air and He gas pressure is shown in Fig. 8.12. One can see that for the pressure range of $10^3 < p < 10^4$ Pa of air and $6 \times 10^3 < p < 2 \times 10^4$ Pa of He, ~30 and ~50%, respectively, of the power reaches the output of the Pyrex tube through self-channeling. Outside these pressure ranges, one can assume that the plasma density formed during the ~0.5 ns long HPM pulse is too small. At the same time, compared to vacuum, no significant change in the radial distribution of the beam power, measured by the receiving antenna at the output of the Pyrex, was detected.

Typical HPM power envelope, measured by a receiving antenna installed at distance of 120 cm in air (Fig. 8.13a) and He (Fig. 8.13b) for various pressures is shown in Fig. 8.13. In vacuum, microwave power shows a Gaussian temporal profile, identical to the profile of the pulse generated by the SR-BWO. In the pressure ranges, $5 \times 10^2 < p < 10^3$ Pa and $3 \times 10^3 < p < 6 \times 10^3$ Pa for air and He, respectively, the waveform of the power changed significantly showing the double hump structure separated by 0.5–0.8 ns, as expected in section "Microwave Pulse Self-channeling in a Preliminarily Formed Low-Density Plasma". For the pressure ranges, $10^3 < p < 10^4$ Pa and $6 \times 10^3 < p < 2 \times 10^4$ Pa for air and He, respectively,

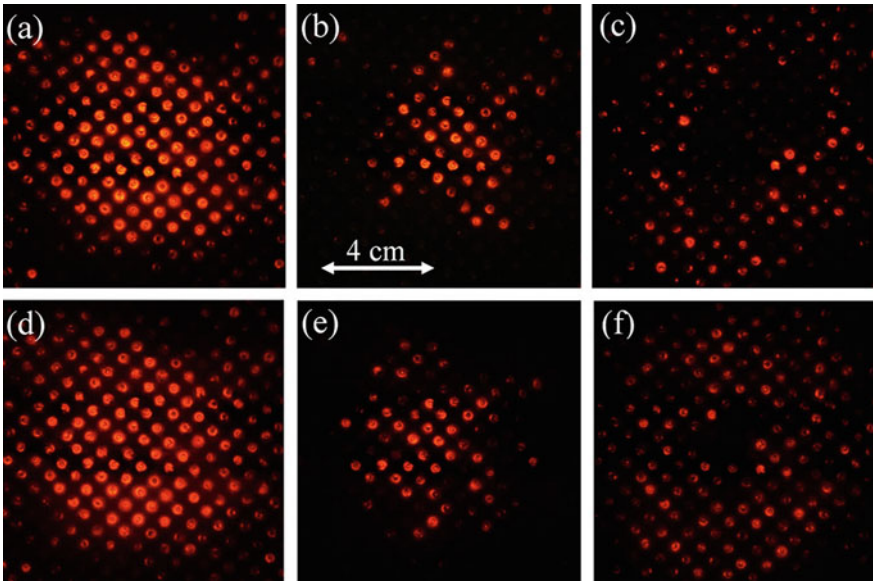

Fig. 8.11 Time integrated patterns of the HPM pulse qualitative power distribution, measured by the array of Ne lamps at the distance of 10 cm from the focal plane: **a** He: 20 mPa; **b** He: 4.5×10^3 Pa; **c** He: 3×10^4 Pa; **d** air: 10^5 Pa; **e** air: 7×10^2 Pa; **f** air: 10^4 Pa [7]

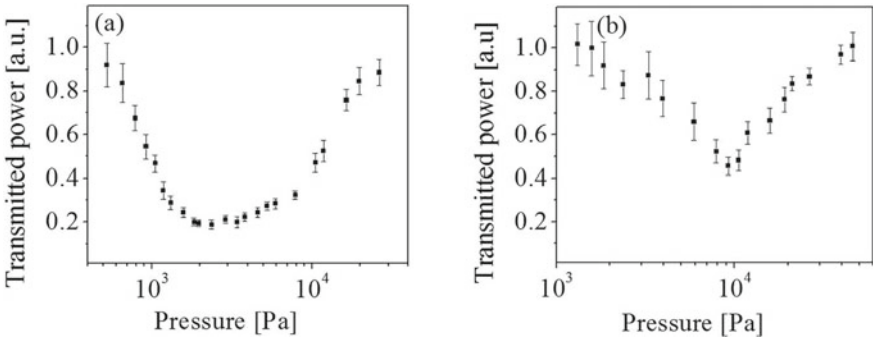

Fig. 8.12 Transmitted microwave power, measured at the receiving antenna, versus the gas pressure, for air (**a**) and He (**b**) [7]

the measured power waveforms were irregular and it was difficult to distinguish two peaks. One can assume that within these pressure ranges, at near- or over-critical density plasmas blocked most of the power with strong microwave reflection and scattering reaching the receiving antenna. At higher pressures, $p > 10^4$ Pa in air and $p > 2 \times 10^4$ in helium the temporal profile of the microwave power is similar to that in vacuum. It seems reasonable to assume that ionization is suppressed at high

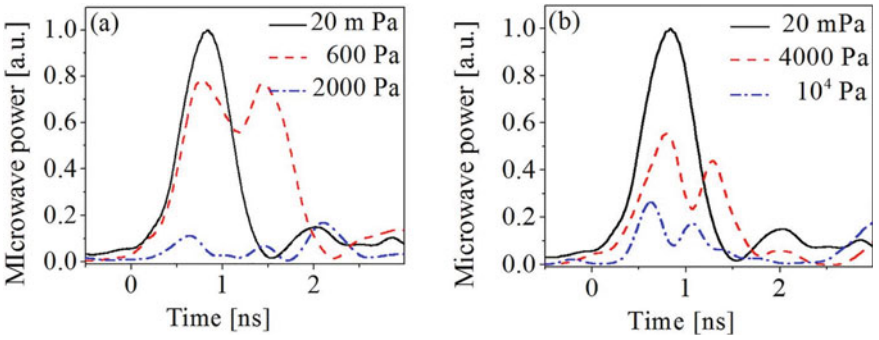

Fig. 8.13 Typical temporal dependence of the power of the transmitted signal, measured at the receiving antenna, for different pressures of **a** air and **b** He. The amplitude of the power is normalized to the peak power in vacuum [7]

pressure when the electron mean free path is small and an avalanche ionization does not develop.

The energy of the plasma electrons was estimated by measuring the luminescence generated by their interaction with thin aluminum foil covering plastic scintillators. A scintillator, coupled to an optical fiber, was placed at the focal plane with a distance of $r = 4.5$ cm from the axis of the Pyrex tube. In Fig. 8.14, typical luminescence signals at aluminum foil of thickness 10 and 20 μm are shown. No luminescence was observed for 30 μm thickness. Stopping range data for electrons in Al suggests the presence of plasma electrons of energies ~15 keV. The presence of such high energy electrons can only be the result of the high electric fields within the focal region. Results similar to those seen in Fig. 8.15 were obtained in air within the pressure range $5 \times 10^2 < p < 6 \times 10^3$ Pa. Outside this range, for both lower and higher pressures, the luminescence signal was below the noise level of the photomultiplier tube used.

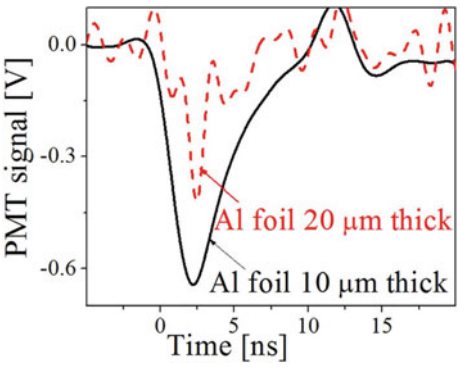

Fig. 8.14 The luminescence signal from the fast plastic scintillator covered by a 10 μm thick Al foil (solid back line) and by a 20 μm (dashed red line), positioned at $r = 4.5$ cm from the axis of the Pyrex tube at the focal plane, for air at $p = 1.5 \times 10^3$ Pa [7]

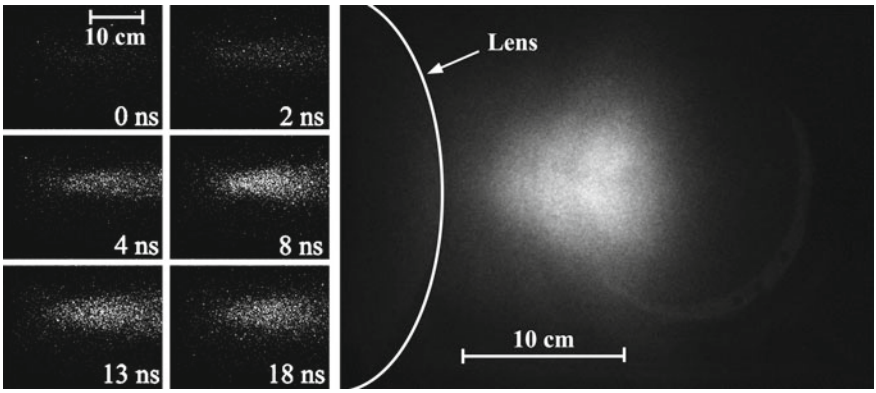

Fig. 8.15 (Left) Fast framing images (1.2 ns exposure time) of Ar plasma light emission during and after the HPM pulse propagation in rf plasma (gas pressure of ~1.5 Pa) with preliminary density of $\sim 7 \times 10^{10}$ cm^{-3}. 0 ns corresponds to the pulse entrance time at $z = 0$ (tip of the lens). (Right) Fast framing image (10 ns exposure time) of the plasma light emission at $t = 10$ ns and gas pressure of ~20 Pa [8]

Interaction with a Preliminarily Formed Low-Density Plasma

A detailed description of the results of the experiments with a 9.6 GHz, 500 MW HPM pulse interacting with a preliminarily formed plasma are presented in Ref. [7]. Fast framing images, of the Ar plasma light emission following the propagation of the HPM pulse are shown in Fig. 8.15 (left). A radially-confined, well-defined more than 30 cm long plasma column of 5 cm diameter is observed. The length of this plasma column is ~6 times longer than the Rayleigh length for beam propagation in vacuum. Similar images were obtained for He plasma with density of $\sim 2.6 \times 10^{11}$ cm^{-3} at the focal plane of the dielectric lens for gas pressure of ~50 Pa. Formation of this narrow plasma channel suggests self-channeling of the microwave beam similar to that described in section "Interaction with a Neutral Gas" of HPM pulse interaction with neutral gas [10, 11]. Note that self-channeling was observed only within the density ranges of $(2 - 3) \times 10^{11}$ cm^{-3} and $(1.5 - 5) \times 10^{11}$ cm^{-3} for He and Ar rf plasmas, respectively. A sharp cutoff of the plasma channel at $z = 13$ cm was observed when the plasma density is large [see Fig. 8.15 (right)]. For smaller density plasma, plasma light emission was not sufficient for visual observation.

The total energy (in arbitrary units) collected by the front and side antennas (see Fig. 8.1), i.e. the transmitted and scattered energy, respectively, for different initial plasma densities are shown in Fig. 8.16b. Similar results were obtained for Ar plasma at a gas pressure of 1.5 Pa. Increase in the density of initial plasma up to $n_p \sim 2.2 \times 10^{11}$ cm^{-3}, leads to the increase in the scattered integrated energy which becomes almost equal the value of transmitted power in vacuum ($n_p = 0$). At the same time, the transmitted integrated energy reduces considerably. The reason for this is the plasma, created by the HPM pulse at the focal plane of the lens. This plasma enhances the microwave scattering and decreases the transmitted energy.

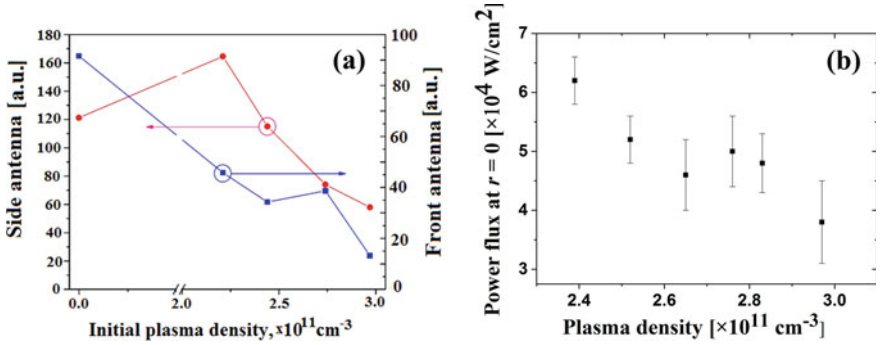

Fig. 8.16 **a** The total energy (in arbitrary units) received by the side (left scale) and front (right scale) antennas as a function of the initial plasma density. **b** Transmitted microwave power density measured on the axis ($r = 0$ cm) and $z = 140$ cm versus preliminary plasma density for 50 Pa neutral He [8]

As the initial plasma density increases above 2.2×10^{11} cm^{-3}, the scattered energy decreases gradually, as well as the transmitted energy (Fig. 8.16a panel), decreases up to ~2.65×10^{11} cm^{-3}. However, the further increase in the initial plasma density leads to transmitted energy increase appreciably. The absolute values of the transmitted microwave power measured by the front antenna versus the initial plasma density are shown in Fig. 8.16a. One can see clearly increase in the transmitted power at initial plasma density of 2.8 ± 0.1 cm^{-3}. These data can be explained by the hollow plasma channel formation in the focal region. This channel traps essential cross-section of the pulse, reduces the beam divergence, and, as a result, increases the power delivered to the front antenna.

For Ar plasma, in Fig. 8.17a, the plasma light emission intensity measured by the collimated PMTs (see Fig. 8.1) at $z = 40$ cm and at the lens focal position at $z = 9$ cm is presented. The HPM pulse interaction with plasma leads to the expected sharp increase in the plasma light emission intensity due to the increased energy and density of the plasma electrons [8]. This increased light emission decays to its initial level within several hundreds of nanoseconds. The ratio between the peaks in the plasma light intensities measured at $z = 40$ cm and $z = 9$ cm (see Fig. 8.17b) increases with increasing preliminary plasma density. This can be associated to the larger power of the beam at $z = 40$ cm at increased density of the preliminary plasma, manifesting a self-guiding effect.

Summary of Experimental Results

In the experiments described above, we studied the non-linear interaction of a high-power, sub-ns X-band focused microwave beam with a low-pressure neutral gas and a preliminarily formed low density plasma using microwave, optical, and spectroscopic methods. Results of these studies showed that within certain gas pressure ranges with

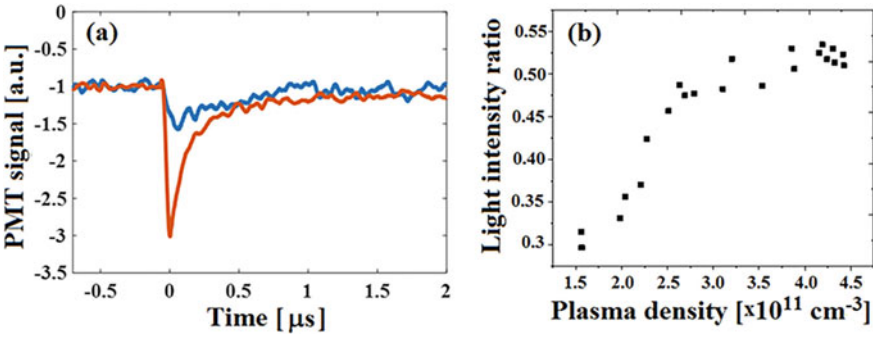

Fig. 8.17 **a** Light emission from the plasma obtained at z = 40 cm (blue) and z = 9 cm (red) for preliminary Ar plasma of 4.4×10^{11} cm^{-3}. **b** Dependence of the plasma light intensities ratio obtained at z = 40 and z = 9 cm versus the density of the preliminary plasma density. Zero time corresponds to the microwave beam propagation through the plasma [8]

specific type of gas, the plasma near the beam axis with considerably lower density than the beam periphery. This leads to the formation of guiding channel through which the beam self-focuses. Outside these pressure ranges, plasma formation shows either diffuse or stream-like. Energetic electrons, which been accelerated by the HPM beam, with energy about 15 keV were also detected. Also, it is found that an initial radially inhomogeneous distributed plasma profile leads the ionization-induced self-channeling of the microwave beam occurs for significantly lower HPM field intensity.

8.2.4 Particle-In-Cell (PIC) Simulations Resulting in Self-channeling

To support the experiment and the theoretical model we performed PIC simulations using the hybrid LSP (Large Scale Plasma) code [27–29]. We performed simulation for a 10 GHz, 500 MW, 0.5 ns duration HPM pulse introduced into a volume at the axial point $z = 0$ and focused to a focal plane at $z = 18$ cm to a beam shaped with a spatial Gaussian distribution with a 2.3 cm FWHM (Full Width Half Maximum) waist. The simulation volume was filled uniformly with neutral He gas of density $n_g = 1.64 \times 10^{17}$ cm^{-3}. We assumed that ionization is due to electron impact ionization by a uniformly distributed small density ($n_0 = 10^6$ cm^{-3}) background cosmic electrons. We account in the simulations for electron impact ionization, and four of the most important electron-He excitation reactions using the cross-section functions given in [26]. This entire electrodynamical process is followed up to less than 10 ns so that we assume that atoms and ions are stationary and only the dynamics of electrons is followed.

In Fig. 8.18 one can see that after a relatively long time (~4.5 ns) following the injection of the microwave beam, the gas ionizes to critical plasma density levels (~10^{12} cm^{-3}) but these high levels develop into a high density "hollow" tube with increasing length, until finally at ~6 ns critical density starts to close this open channel. This behavior has been predicted by Bogomolov et al. [24] and modeled in "Microwave Pulse Self-channeling in a Neutral Gas".

In Fig. 8.19 we follow the microwave beam's propagation though this self-made channel. Note that the length of the propagation through the channel is considerably longer than the Rayleigh length, of the same order of magnitude as that observed in the experiment (see Fig. 8.9).

In Fig. 8.20 the plasma electron energy distribution in space is drawn at the same times as those in Figs. 8.18 and 8.19. The electrons can reach an energy of the order of several keV which confirms the energies observed in the experiment (Fig. 8.14).

Next, we present LSP simulations where the focused microwave pulse encounters a mixture of a background He gas at a pressure of 150 Pa and a 2.75 × 10^{11} cm^{-3} uniform density He plasma and a non-uniform density plasma at the focal plane as given by Eq. 8.2.7 in section "Microwave Pulse Self-channeling in a Preliminarily Formed Low-Density Plasma". Some other plasma density distribution details were also accounted for following the experimentally measured distribution (i.e. Fig. 8.5).

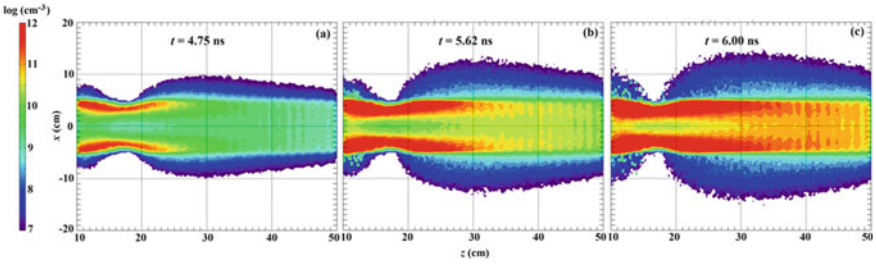

Fig. 8.18 Time- and space-resolved evolution of the density of the plasma generated by microwave beam ionization of He during beam propagation obtained by LSP simulations [7]

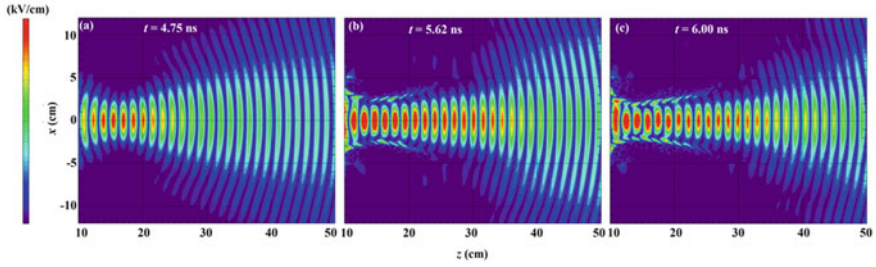

Fig. 8.19 Temporal- and spatial-resolved evolution of the microwave electric field $|E_x|$ of the propagating HPM beam obtained by 3D LSP simulations. The electric field in **a** is between 0 and 200 kV/cm, whereas in **b** and **c** 0–150 kV/cm and the contour colors scale accordingly [7]

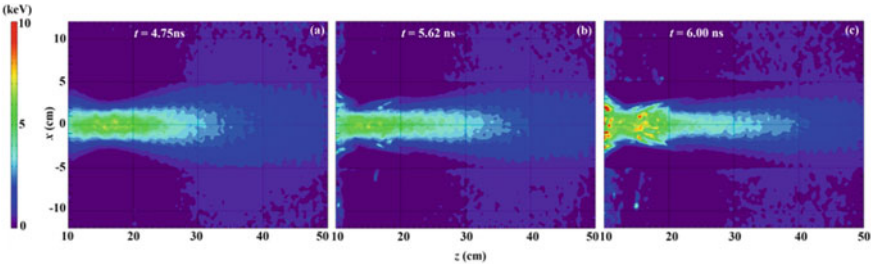

Fig. 8.20 Time- and space-resolved evolution of the plasma electron energy during the propagation of the microwave beam [7]

In Fig. 8.21, following the theoretical model, we consider two cases. When the plasma is uniform (Fig. 8.21d–e) channeling starts but it fills in very quickly. For a non-uniform initial plasma density accounting for the convex shape of the focusing lens (Fig. 8.21a–c), the plasma channel is clearly observed. In Fig. 8.22 the time and space resolved propagation of the microwave beam is drawn. When the plasma is non-uniform (Fig. 8.21a–c) channeling, dispersion out from channel and scattering from the channel walls are observed. Note the scattered wave which leaves the focal region at an angle to the main wave beam propagation. In the experiments, this wave was registered by the side antenna. When the plasma is uniform all these have smaller footprints (Fig. 8.22d–e). For a non-uniform plasma but no other processes (neutrals ionization and excitations) the focused beam simply disperses from the focal region which proves that the presence of plasma is not sufficient for self-channeling to appear.

8.3 Wakefield in a Plasma-Filled Waveguide

The excitation of space-charge oscillations in under-dense plasmas by an ultra-short intense laser pulse resulting in a wakefield formation is perhaps the most noticeable example of a wave-plasma interaction. This physical phenomenon, being interesting by itself, holds the greatest promise for charged particles acceleration to the GeV range of energy within a very short distance (of the order of centimeter scale) [30–33]. The accelerating electric field of plasma oscillations excited by the laser pulse grows with the plasma density. In order to exceed significantly the accelerating fields realized in traditional accelerators ($\leq$100 MV/m), the plasma density should be sufficiently large while the frequency of the electromagnetic pulse should exceed the plasma electron frequency. Laser pulses meet these requirements best.

However, the wakefield driven by powerful laser pulses are characterized by very small temporal (ps) and spatial (μm) scales that make experiments investigating the underlying physical processes challenging. Ultrashort HPM pulses can also be used to excite plasma wakes [3]. Similar to laser pulses, to most efficiently excite a

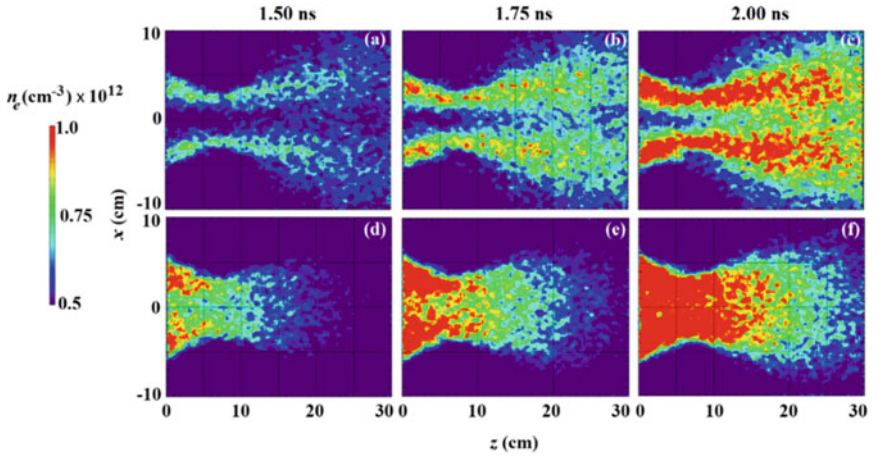

Fig. 8.21 Simulated plasma density contour snapshots, for helium plasma generated by the HPM pulse (135 kV/m, 10 GHz) with an initial non-uniform (**a**–**c**) and uniform (**d**–**f**) radial plasma profile [8]

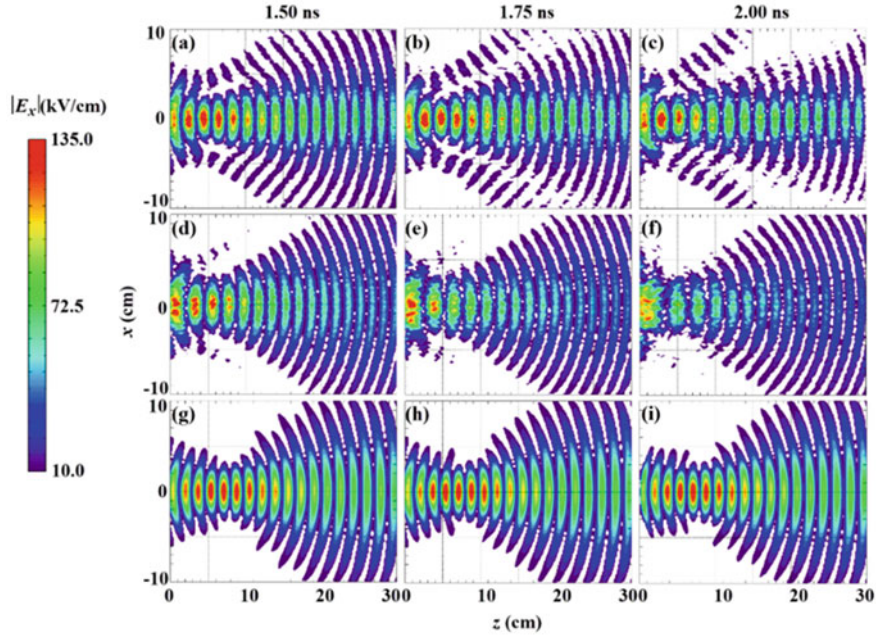

Fig. 8.22 LSP calculated snapshots of the focused HPM beam (135 kV/cm, 10 GHz). Absolute values of $|E_x|(z, x)$ are depicted at $t = 1.50$ ns (**a**, **d** and **g**), 1.75 ns (**b**, **e** and **h**) and 2.00 ns (**c**, **f** and **g**). In **a**–**c** the preliminary plasma fill is non-uniform, in **d**–**f** the uniform and in **g**–**h** a non-uniform plasma is present but no neutral gas or ionizations or excitations exist. The white background in these figures represents electric fields <10 kV/cm [8]

plasma wake, the HPM pulse duration should be approximately equal to one half the Langmuir electron oscillation period. For instance, for a pulse duration of ∼0.5 ns, the optimal plasma electron density is $\sim 10^{10}$ cm^{-3}. For this case, the wakefield amplitude expected from HPM-plasma interaction will be several orders lower than those excited by powerful ultrashort laser pulses. However, the wakefield excited by a microwave pulse is characterized by significantly larger temporal and spatial scales. This allows the application of different more conventional time- and space- resolved diagnostic tools to measure the plasma parameters, which determine the formation and evolution of the wake, and comparison between experimental and theoretical results.

Recently, there has been interest in the excitation of wakefields by electromagnetic pulses with more complex than linear or circular polarization and non-Gaussian transverse profiles. In particular, wakefields excited in a plasma-filled rectangular waveguide by the TE mode of a microwave pulse were studied in Refs. [34, 35]. The field structure of the driving electromagnetic pulse in a waveguide strongly differs from that in unbounded plasma. The electromagnetic energy is concentrated in a small transversal cross-sectional area along the entire waveguide and the angular divergence of the wave is limited by the waveguide walls.

In this section, the wakefield excitation by an HPM pulse of a TM mode propagating in a cylindrical waveguide filled with plasmas is considered. This choice of the operating mode allows one to use the electromagnetic wave generated by the SR-BWO directly, without mode converters.

8.3.1 Experimental Arrangement for Wakefield Excitation

The experimental investigation of wakefield excitation by a microwave pulse propagating in a plasma-filled waveguide has been performed using two different SR-BWO as the HPM pulse source. The 9.6 GHz, 0.35 ns long, 200 MW source was described in Sect. 8.2.1. The second source produces a pulse of the same duration, but higher power, up to 1.2 GW, and 25.5 GHz carrier frequency (for details, see Ref. [1]).

For studying the HPM pulse propagation through a plasma-filled waveguide, a flashboard plasma source [36] was developed and characterized. The plasma on a flashboard is produced by surface flashover between the many electrodes placed a dielectric surface. To the back side of this dielectric sheet, a conducting grounded electrode is attached. In the design presented below, four flashboards were installed on the inner surface of a 900 mm long, 90 mm diameter stainless steel tube. At side of the tube, two 500 mm × 10 mm observation slots were carved and covered by transparent windows for diagnostic purposes (see Fig. 8.23a). When a high voltage (HV) pulse is applied, a surface flashover occurs between the multi-electrodes gaps (see Fig. 8.23b). The generated plasma accelerated by the self-magnetic field gradient of the discharge current in the direction outwards from the surface. The accelerated plasma flows overlap and fill the entire volume of the tube. Each flashboard was

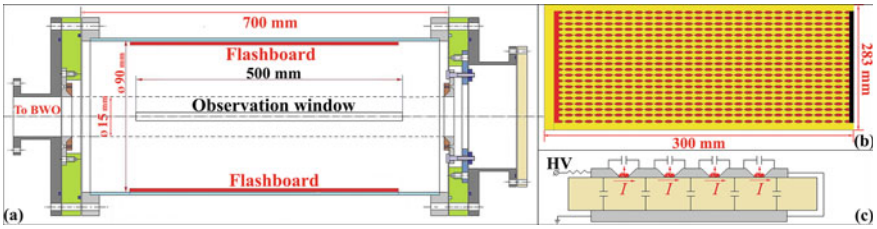

Fig. 8.23 **a** Drawing of the experimental chamber with the installed flashboards and **b** a flashboard and **c** its corresponding simplified equivalent electrical circuit [11]

manufactured from a 300 mm × 283 mm PCB, with 10 mm × 6 mm electrodes and 1.5 mm gaps. The distance between electrode lines is 10 mm.

The flashboard is driven by a 20 kV, 12 kA and ~1.5 μs long pulse. This high-voltage pulse is produced by a 400 nF capacitor discharge. In order to avoid an underdamped discharge, low inductance resistors (1.5 Ω) were connected in series to each of the flashboard chain's HV input points. The produced plasma light emission was observed by an intensified fast-framing camera (Stanford Optic Inc. 4QuikE) observing from the front and side of the tube. The temporal evolution of the plasma density is characterized by various diagnostic methods, including the microwave cut-off/interferometry and time-resolved visible spectroscopy. The plasma distribution along the tube axis was obtained by a biased Faraday cup array. Examples of front and side images of the plasma light emission are shown in Fig. 8.24. The front images (Fig. 8.24a) show that the plasma light emission forms at the outer periphery, and in time, it fills the entire volume with maximal light intensity on axis, the result of the converging plasma flow. Uniformity of the plasma light emission is obtained after ~5 μs in both transverse and side views.

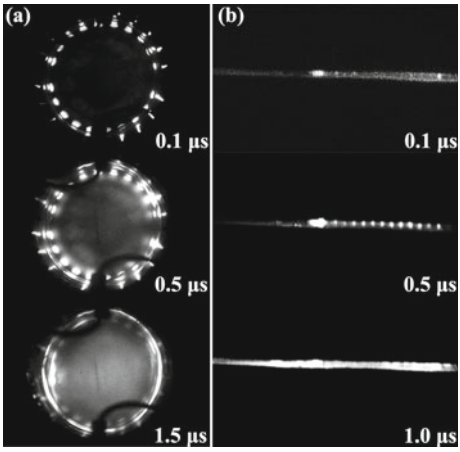

Fig. 8.24 Front (**a**) and side (**b**) images of the flashboard plasma light emission at various times [11]

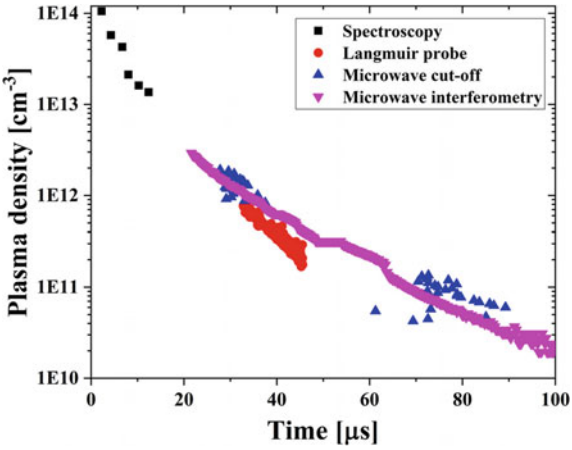

Fig. 8.25 Time dependence of the flashboard plasma density measured by different diagnostic methods [11]

The temporal evolution of the plasma density measured by various diagnostic methods is shown in Fig. 8.25. Time-resolved visible spectroscopy, microwave cut-off and interferometry, and single Langmuir probe measurements are in good agreement. The results in Fig. 8.25 show that the flashboard source produces a spatially uniform plasma over a broad and controllable plasma density range (10^{10}–10^{14} cm^{-3}).

A constant plasma density within this range can be chosen to fill uniformly either a 28 mm (for experiments using the 9.6 GHz microwave pulse) or 14 mm diameter (for the 25.5 GHz SR-BWO) cylindrical waveguides (see Fig. 8.26) by changing the time delay between the beginning of the plasma formation and the injection time of the microwave pulse. This waveguide is connected directly to the output of the SWS and is placed coaxially inside the vacuum tube containing the flashboards. To allow plasma to fill the waveguide for the 9.6 GHz case the waveguide consisted of thin (1 mm diameter) stainless steel wires spaced 1 mm apart (see insert in Fig. 8.26a). The wire-waveguide has a ~60% geometrical transparency, not affecting the plasma convergence through the gaps between the wires. MAGIC electromagnetic simulations show that the wires are placed sufficiently close so that very little microwave power leaks through. For the 25.5 GHz SR-BWO only part of the waveguide consisted of 250 mm long slots spaced 1.5 mm apart.

The complete experimental setup used in experiments with 9.6 and 25.5 GHz HPM pulses interaction with preliminarily formed plasma is shown in Fig. 8.26. The output end of the microwave source is directly connected to a directional coupler [37] (#1 in Fig. 8.25a). The waveguide is installed on the axis of the flashboard plasma chamber and connected to a second coupler at the downstream end of the plasma chamber (#2, Fig. 8.26a). The plasma density in an experiment can be fixed in the range of 10^{10}–10^{12} cm^{-3} by choosing the microwave beam's switch on after a delay time from the flashboard discharge according to the calibration seen in Fig. 8.25. Optical fibers, with one end covered by thin aluminum foils attached a fast PMT (rise-time ~0.5 ns), were used to collect and estimate the maximal energy of ejected

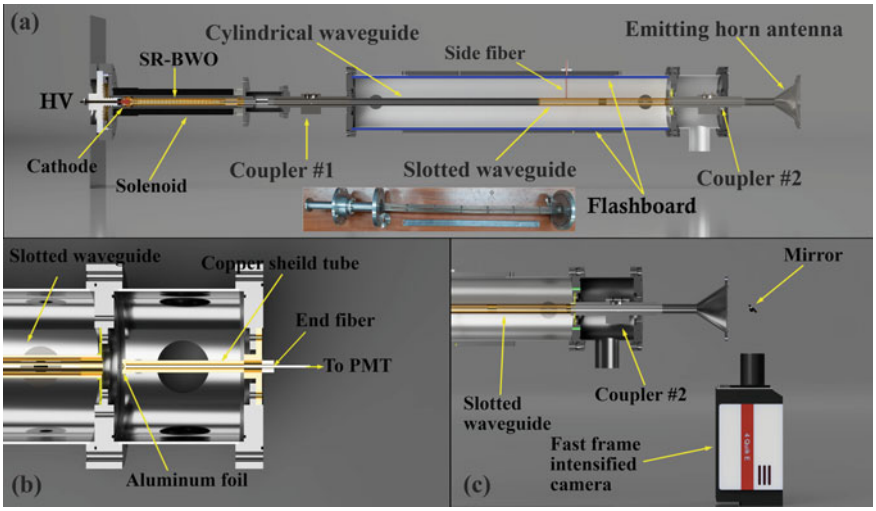

Fig. 8.26 Schematic drawing of the experimental apparatus. **a** Vacuum chamber containing the waveguide with slots. Flashboards along the chamber walls and diagnostic apparatus are pointed out. Enlarged left side end of (**b**), with either a fiber or Faraday cup or **c** with an intensified 4QuikE camera protected against microwave radiation by a water filter attached to the waveguide end [13]

electrons by using NIST data [38] for various thickness Al foils and measuring the resulting luminescence induced in the fiber. These measurements were carried out inside the flashboard tube at various points along the waveguide, observing the effect of the propagating microwave. To study the time-resolved plasma light emission, light collecting fibers coupled to PMT were installed outside the vacuum chamber in front of the Perspex window. The current and the energy of electrons leaving the waveguide downstream, were measured by a Faraday cup with a 3 cm diameter graphite collector. The entrance of the Faraday cup is covered with different thickness Al foils. A 4QuikE camera was used to observe the plasma light emission pattern when the HPM pulse interacts with the plasma. The camera was placed at the output of the tube and focused on the mid-plane of the plasma filled region in the waveguide.

To maintain the background vacuum at a pressure of ~5 × 10 mPa, two turbo-molecular pumps were used. After the flashboard discharge, the pressure increasing up to 4 Pa within ~20 μs, is measured by a calibrated Penning vacuum probe installed inside the experimental tube. This pressure increase is caused by the intense gas desorption and surface erosion of the flashboard's operation.

8.3.2 Wakefield Excitation in a Waveguide Filled with Plasma. Theoretical Analysis

Electron Motion in the Waveguide Eigenmode's Electromagnetic Fields

Hereafter we shall assume that the electromagnetic pulse contains many oscillations, i.e.,

$$\omega t_{pulse} \gg 1. \tag{8.3.1}$$

Our prime interest here is with the plasma, whose electron Langmuir frequency, ω_p, relates to the pulse duration as $\omega_p t_{\text{pulse}} \sim 1$, so that

$$\omega_p \ll \omega. \tag{8.3.2}$$

The last inequality means that one can neglect disturbances of the waveguide eigenmode's fields, caused by the presence of plasma, so that the fields of the TM_{01} mode are

$$\begin{cases} E_r = E_0(z,t)J_1(k_\perp r)\sin(\omega t - k_z z), \\ H_\phi = \frac{k_0}{k_z}E_0(z,t)J_1(k_\perp r)\sin(\omega t - k_z z), \\ E_z = -\frac{k_\perp}{k_z}E_0(z,t)J_0(k_\perp r)\cos(\omega t - k_z z). \end{cases} \tag{8.3.3}$$

Here $k_0 = \omega/c = \sqrt{k_z^2 + k_\perp^2}$, $k_\perp = \gamma_{01}/R$. γ_{01} is the first order solution of the Bessel function J_0, and R is the waveguide radius. Equation (8.2.3) describes a wave packet (pulse), when the amplitude E_0 is a slowly varying function of the argument $t - z/v_g$, where $v_g = d\omega/dk_z$ is the wave group velocity.

The mode fields Eq. (8.2.3) contain two spatial scales: the wave period $T = 2\pi/\omega$ and the pulse duration t_{pulse}, $t_{\text{pulse}} \gg T$. When the dimensionless amplitude $\mathcal{E} = eE_0/mc\omega \ll 1$ is small enough, then for small electric fields the electron motion in the pulsed fields can also be presented as an oscillatory motion with slowly varying parameters. The oscillating part is proportional to $\mathcal{E}$, while the slowly varying parts are proportional to $\mathcal{E}^2 \ll \mathcal{E}$.

Omitting straightforward calculations (see Ref. [3] for details), let us present the equations which describe the slow motion of the electron:

$$\begin{cases} \frac{d\beta_\xi}{d\tau} = \frac{1}{2}\left[\sin^2\psi\left(1 + \frac{1}{2\cos^2\psi}\right)J_0^2(\rho) + \left(\frac{1}{2} - \sin^2\psi\right)J_1^2(\rho)\right]\frac{d\mathcal{E}^2(\theta)}{d\theta}, \\ \frac{d\beta_\rho}{d\tau} = \frac{1}{2}\sin^2\psi\,\mathcal{E}^2(\theta)\left[\left(\frac{1}{\cos^2\psi} - 2\right)J_0(\rho) + \frac{1}{\rho}J_1(\rho)\right]J_1(\rho), \\ \frac{d\xi}{d\tau} = \beta_\xi,\ \frac{d\rho}{d\tau} = \beta_\rho. \end{cases} \tag{8.3.4}$$

Here the following dimensionless variables and parameters are introduced: $\tau = \omega t$, $\xi = k_z z$, $\beta_\xi = k_z v_z/k_0 c$, $\beta_\rho = k_\perp v_r/k_0 c$, $\sin\psi = k_\perp/k_0$, $\cos\psi = k_z/k_0$, and $\theta =$

$\tau - \xi/\cos^2\psi$. The right-hand sides of Eqs. (8.2.4) represent the forces experienced by the electron in the longitudinal and radial directions, respectively. The longitudinal force is proportional to $d\mathcal{E}^2/d\theta \propto \tau_p^{-1}\mathcal{E}^2$, where $\tau_p = \omega t_{\text{pulse}} \gg 1$. In contrast, the radial force does not contain a derivative of $\mathcal{E}^2$.

When the wavelength is of the same order of magnitude as the waveguide radius, i.e., $\sin\psi \sim 1$, the longitudinal force exceeds the radial force only near the axis, where $\rho \cong \tau_p^{-1} \ll 1$. Moreover, the longitudinal force as a function of time changes its sign, while the radial force is independent of time and is defined only by the radial position. This means that almost all electron are forced out from the waveguide mainly in the radial direction by the electromagnetic pulse. Note that in a super-dimensional waveguide ($\sin\psi \to 0$), the longitudinal force dominates. The tracing of the origin of the right-hand terms in Eq. (8.2.5) allows one to separate the ponderomotive and Lorentz forces:

$$\frac{d\beta_\rho}{d\tau} = \frac{1}{2}\sin^2\psi\, J_1(\rho)\left\{\underbrace{-\left[2J_0(\rho) - \frac{1}{\rho}J_1(\rho)\right]}_{\text{gradient force}} + \underbrace{\frac{1}{\cos^2\psi}J_0(\rho)}_{\text{Lorentz force}}\right\}. \tag{8.3.5}$$

The Lorentz force (always positive) tends to move electrons to the waveguide walls. The direction of the total radial force can be either towards the waveguide wall or opposite to the Lorentz force depending on waveguide radius. The ponderomotive (gradient) force is negative near the axis and becomes positive after the maximum of $J_1(\rho)$, closer to the waveguide wall. If on axis, the gradient force is smaller than the Lorentz force, then the total radial force is positive along the entire waveguide radius. Thus, for $\cos^{-2}\psi > 1.5$, the radial force is always positive, and a critical radius can be defined as $R_{\text{cr}}[\text{cm}] = \frac{19.85}{f}[\text{GHz}]$ so that for waveguide radii $R < R_{\text{cr}}$ the electromagnetic pulse forces all electrons out towards the walls whereas when $R > R_{\text{cr}}$, part of the electrons are moved toward the axis, others move in the opposite direction, towards the waveguide wall.

Space Charge Field

So far, only single electron motion was considered. The plasma electrons are pushed out of their equilibrium position by the microwave pulse. The space charge of the immobile plasma ions produces an electric field. The electron density longitudinal modulation's spatial scale is of the order of the pulse length $v_g t_{\text{pulse}}$, which is significantly larger than the waveguide radius making the radial component of the space charge electric field much stronger than the axial field. Therefore, only the radial component $E_r^{(\text{pl})}$ of the space charge field will be considered.

Let us assume that the radial electron trajectories of the electrons do not intersect. This means that before the pulse's passage, the total charge of electrons, Q_e, contained initially in a given cross-sectional circle of radius r_0 remains constant: $Q_e(t) =$

$e\pi r_0^2 n_0 = e\pi r^2(t) n(t)$, where n_0 is the unperturbed plasma density. The total charge of ions contained in the circle of radius $r(t)$ is $Q_i = -e\pi n_0 r^2(t)$. The total charge contained in the circle of radius $r(t)$ is $Q_e(t) - Q_i(t) = e\pi n_0\left[r_0^2 - r^2(t)\right]$. Thus,

$$2\pi r(t) E_r^{(\mathrm{pl})} = 4\pi^2 e n_0\left[r_0^2 - r^2(t)\right]$$

or

$$\mathcal{E}_r^{(\mathrm{pl})}(\tau) \equiv \frac{eE_r^{(\mathrm{pl})}}{mc\omega} = \frac{\nu^2}{2\sin\psi}\left[\frac{\rho^2(0)}{\rho^2(\tau)} - \rho(\tau)\right]. \tag{8.3.6}$$

Here, $r(t)$ is the trajectory of an electron initially at a radial position r_0, and $\nu = \omega_p/\omega \ll 1$. Now, Eq. (8.2.5) for electron motion, using Eq. (8.2.6), can be written as:

$$\begin{aligned}\frac{d\beta_\xi}{d\tau} = \frac{1}{2}\left[\sin^2\psi\left(1 + \frac{1}{2\cos^2\psi}\right)J_0^2(\rho) + \left(\frac{1}{2} - \sin^2\psi\right)J_1^2(\rho)\right]\frac{d\mathcal{E}^2(\theta)}{d\theta} + \cdots \\ \cdots + \frac{\nu^2}{2\sin\psi}\left[\frac{\rho^2(0)}{\rho^2(\tau)} - \rho(\tau)\right].\end{aligned} \tag{8.3.7}$$

Numerical Solutions

The MW pulse propagating through the plasma displaces only the electrons from their equilibrium positions with ions serving as a static background positive charge. When the microwave beam propagates through the waveguide, the electric field caused by the separated charges tends to pull the electrons back to their initial positions. Due to inertia, the electrons pass the equilibrium position and are focused either near the axis (Fig. 8.27a), when $R < R_{\mathrm{cr}}$, leading to significant density modulation, or somewhere between the axis and the wall for $R > R_{\mathrm{cr}}$ (Fig. 8.27b). The structure and the amplitude of the wakefield can be controlled by the value of the waveguide radius. It is worth noting that part of the electrons is pushed out to the waveguide wall and absorbed, so that the plasma becomes positively charged after the pulse passage.

In Fig. 8.28 results of 3D PIC calculations using the Large Scale Plasma (LSP) [27, 39] code are presented. The contour plots [Fig. 8.28 (upper panel)] are for waveguides of different radii filled with electrons and immobile ions plasma of 2.5 $\times$ 10^{10} cm^{-3} initial density, 3 ns following the injection of a 28 GHz, 500 MW and 0.4 ns (FWHM) microwave pulse in a TM_{01} mode at $z = 0$. The simulated results agree qualitatively with the 1D model, but the density modulation is less pronounced.

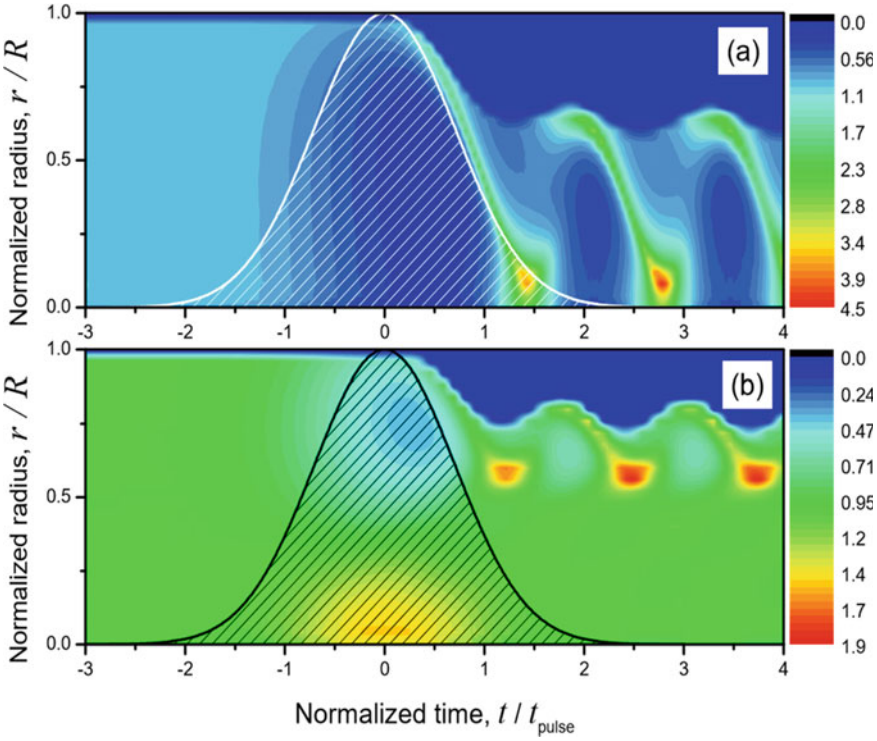

Fig. 8.27 Time dependent evolution of the normalized electron density for different waveguide radii. The initial plasma density is $n_0 = 2.5 \cdot 10^{10}$ cm^{-3}, the microwave power $P = 600$ MW, and the frequency $f = 28$ GHz and 0.4 ns pulse duration. The time $t = 0$ corresponds to the center of the Gaussian pulse (shown as a shadow area). The wakefield itself is a periodic modulation of the electron density which remains in the waveguide after the pulse passage. **a** $R = 0.66$ cm; **b** $R = 0.8$ cm

8.3.3 Phenomena Accompanying a Powerful Electromagnetic Pulse Propagation Along a Plasma-Filled Waveguide

The propagation of a powerful electromagnetic pulse along a plasma-filled waveguide is accompanied by several specific effects which are not inherent to unbounded plasma. The experimental confirmation verifying the theoretical models of these effects require specific diagnostic methods.

Fast Electron's Flux Through the Waveguide's Side Boundary

The wall of the waveguide, used in the experiments, is partially transparent to electrons and almost opaque to the microwave field. The microwave pulse ejects part of the plasma electrons through the gaps in the waveguide wall. The one-dimensional

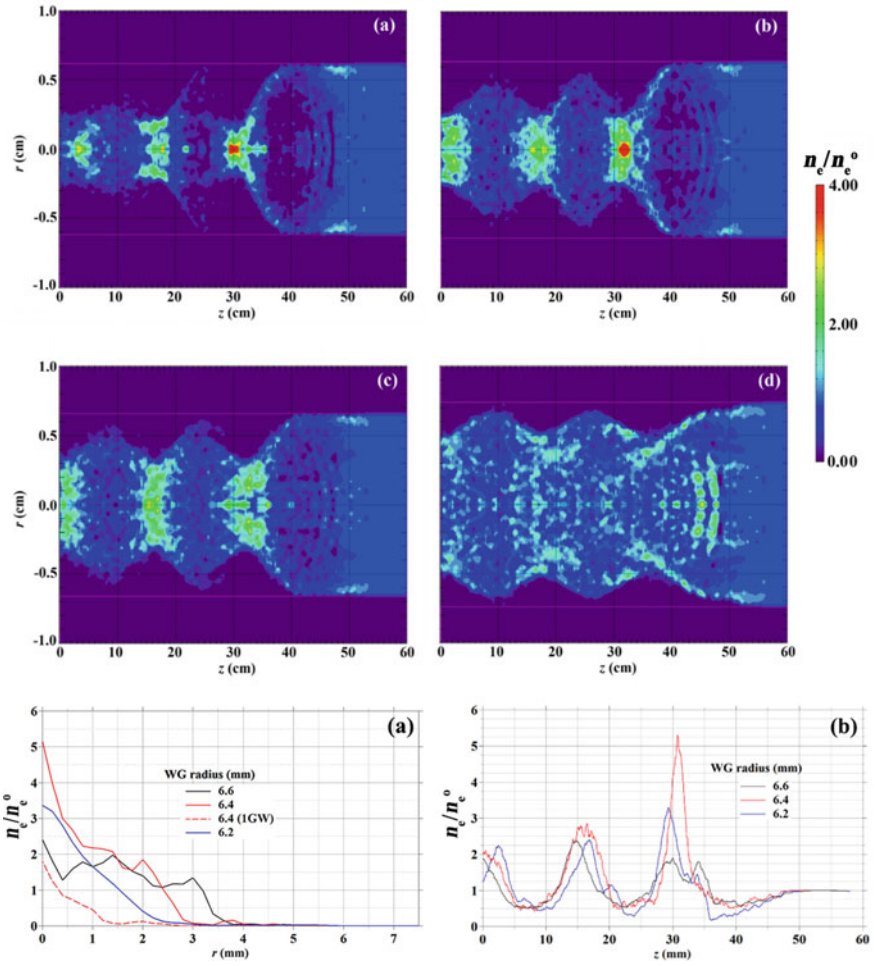

Fig. 8.28 (Upper panel) Contours of the normalized electron densities in plasma filled waveguides of various radii. 6.2 (**a**), 6.4 (**b**), 6.6 (**c**) and 7.5 mm (**d**) 3 ns following the propagation of the high-power microwave pulse. (Lower panel) Radial (at z ~30 cm, the first peak density) **a** and longitudinal ($r = 0$) **b** electron density distribution for the situations seen in the upper panel [11]

model is used to calculate the temporal dependence of the energy of all electrons in the waveguide cross section including those collected on the walls of the waveguide. For the example calculation in Fig. 8.29 (left panel), the high energy electrons reaching 50 keV oscillate inside the waveguide and do not approach the walls. Two kinds of electrons can leave the waveguide through the walls. Firs electrons of energy up to 5 keV which appear as the pulse rises. The second type of electrons, of higher energies, up to 15 keV, appear at the microwave beam's tail. These two types have different origins. The first group originates from electrons initially close to the waveguide wall accelerated by the ponderomotive force toward it. These electrons

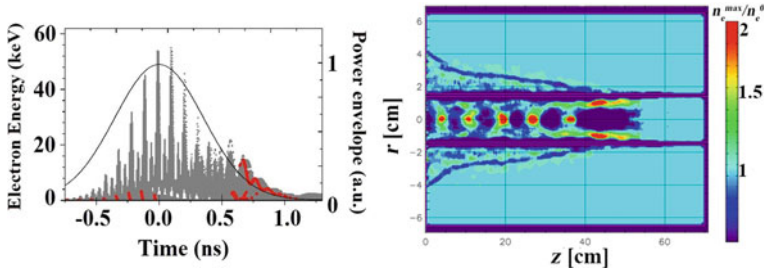

Fig. 8.29 (Left panel) Energies of all electrons in the waveguide cross section versus time calculated by the 1D model (gray), electrons that penetrate through the waveguide boundary (red), and the envelope of the microwave pulse power (black curve) for a plasma density of 5×10^{10} cm^{-3}. Time is measured relative to the maximum of the power [13]. (Right panel) LSP calculated contours of the electron density normalized to its unperturbed value versus z for a 1.4 cm radius, 24-wire array cylindrical waveguide. (9.6 GHz, 500 MW microwave pulse) [3]

are either absorbed or leave the waveguide interior through the experimental slots. Other electrons, which did not reach the boundary, are reattracted toward the axis by the positive space charge field of the uncompensated plasma ions and focus near the axis, as seen in Fig. 8.29 (left panel). This focusing toward the axis is accompanied by strong electron density and space charge electric field fluctuations. During this non-stationary focusing stage, part of the electrons gain sufficiently high energies to overcome the potential barrier created by the ion space charge, and leave through the waveguide walls. These electrons appear in the second group of electrons in Fig. 8.29 (left panel). According to this model, the time interval between these two groups of electrons is close to the pulse duration.

3D-PIC simulations using the LSP code confirmed results of this simple 1-D model. The right panel in Fig. 8.29 demonstrate perturbation of the plasma electrons' density, caused by the pulse propagating (from left to right) along a 24-wire array cylindrical waveguide of 1.4-cm radius. One can see the density perturbations associated with the electrons ejected from the waveguide in the radial direction. Moreover, the LSP simulated electron energies arriving at the waveguide walls reach values of up to ~45 keV and can reach ~100 keV inside the waveguide when collisions and electron impact ionizations with neutrals (a low-pressure background neutral gas, 5×10^{14} cm^{-3} carbon atoms) are included. These results confirm the source of the measured high energy electrons ejected through the space between the wires making up the waveguide.

Wake-Assisted Additional Ionization

In section "Fast Electron's Flux Through the Waveguide's Side Boundary" we showed that wake excitation is accompanied by partial ejection of electrons through the gaps in the waveguide wall. Even complete ejection is possible for higher

microwave power [3]. During the microwave beam's propagation in the waveguide, part of the uncompensated charge of the background ions stays in the waveguide. These electrons oscillate in the potential well created by the uncompensated charge. Eventually, ions drift towards the waveguide boundary and leave or exterior plasma electron are attracted back through the partially transparent waveguide boundary wall, so that in time the potential well disappears. Both these space charge neutralization processes continue long after the beam left the waveguide.

The potential well's depth, $\Delta\varphi$, that is, the energy of the oscillating electrons in the well, depends on the uncompensated positive ion charge density, which for a waveguide radius of 1 cm and plasma density $3\times10^{10}-2\times10^{11}$ cm^{-3}, (as in the experiments) are able to reach several tens of kV for complete electron ejection from the waveguide. Even for incomplete ejection, the remaining electron oscillating energy, is sufficient to ionize the neutrals in the plasma by impact ionization. However, this additional ionization does not change the value of the uncompensated charge. Therefore, all initial and newly created electrons remain trapped in this potential well, and eventually lose their energy on excitation/ionization producing collisions. Thus, behind the microwave pulse the plasma density and the light intensity increase over a certain period of time followed by relaxation. This light's characteristic duration can be orders of magnitude longer than the beam duration.

The temporal growth rate and the maximal value of the plasma density can be estimated by using the following simple model. Assuming homogenous electrons and ions distribution over the waveguide volume, one can calculate the waveguide potential relative to the axis as

$$\Delta\varphi = \pi e R^2 (n_i - n_e). \tag{8.3.8}$$

where n_i and n_e are the ion and electron densities, respectively. One can estimate the kinetic energy of an electron oscillating in the potential well to be $w \approx \Delta\varphi = \pi e^2 R^2 (n_i - n_e)$. Any electron can ionize $N \approx w/\varepsilon_i$ neutrals with an ionization energy ε_i. Thus, the density of the plasma formed by additional ionization can be estimated as $n_p \sim \pi e^2 R^2 (n_i - n_e)/\varepsilon_i$. This density reaches its maximum at $n_e = n_i/2$,

$$\max\{n_p\} \approx \frac{\pi e^2 R^2 n_i^2}{4\varepsilon_i}. \tag{8.3.9}$$

For the experimental conditions mentioned above, one obtains $\max\{n_p\} \sim 10^3 n_i$. Considering that the estimate of Eq. (8.2.9) is very rough, one can still state, with a reasonable level of confidence, that the wake can lead to plasma modulation with densities reaching significantly higher values than the initial density. Note that this can occur only when the beam power is large enough to eject half of the initial plasma electrons from the waveguide.

The above estimate assumes that all electrons have the same maximum allowable energy, $w \sim e\Delta\varphi$, which overestimates the possible increase in the plasma density. For a more precise estimation, it is necessary to know the electron energy distribution $n_e(w)$, oscillating in the potential well. Any ionization event is accompanied by the

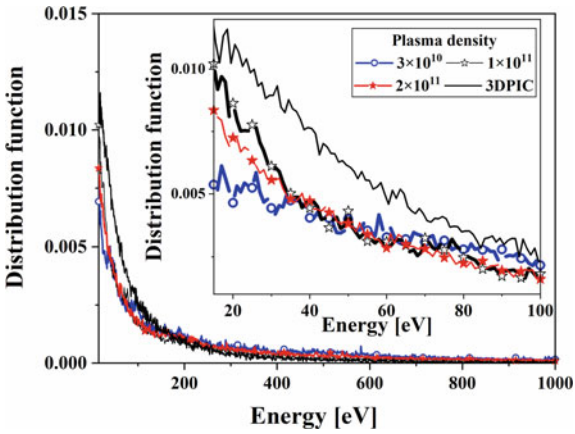

Fig. 8.30 Distribution functions) $n_e^0(w)$ as functions of electron energy for different values of the initial plasma density n_p^0. The lines with symbols are obtained using the 1D model and the solid line is the result of 3D PIC simulations [13]

disappearance of a primary electron from its initial energy interval $[w, w + dw]$ and the appearance of two electrons of lower energies w_1 and w_2, where $w_1 + w_2 = w + \varepsilon_i$. For simplicity, it is assumed below that $w_1 = w_2$, so that both secondary electrons have the same energy. Thus, the variation of the electron density $n_e(w)$ in a given energy interval is given as:

$$\frac{dn_e(w)}{dt} = -n_0 n_e(w) I(w) + 2n_0 n_e(2w + \varepsilon_i) I(2w + \varepsilon_i), \tag{8.3.10}$$

where n_0 is the density of the neutral gas, $I(w) = \sigma_i(w)v$ is the ionization rate with $\sigma_i(w)$ being the ionization cross section and the electron velocity $v = \sqrt{2w/m}$. Equation (8.2.10) should be supplemented by the initial energy distribution of electrons $n_e^0(w)$. Using the 1D model to calculate the electron energy distribution after the HPM has left the system, we found that it is practically independent on the plasma density. In Fig. 8.30 it is shown that both the 1D model and 3D PIC simulation give very similar dependencies on energy above the ionization threshold.

Since the energy distribution is practically independent of the initial plasma density n_p^0, the normalized density $\eta = n_p(t)/n_p^0$ of the newly created plasma is also independent of n_p^0. Moreover, the intensity of light emission, which can be registered by the side fiber (see Fig. 8.26), should be proportional to n_p^0. The numerical solution of Eq. (8.2.10) for the energy distributions shown in Fig. 8.30 and the calculated normalized light intensities obtained in experiments described in Sect. 8.3.4, are presented in Fig. 8.31 and confirm this statement.

It should be noted that the electric field of the uncompensated space charge which confines the electrons, accelerates ions toward the waveguide boundary which in time destroys the potential well for electrons and terminates ionization faster than estimated above.

For the same experimental conditions as experiments, both 1D and 3D simulations estimate that the microwave pulse ejects approximately 30–40% of the electrons through the waveguide slots. The remaining electrons oscillate near their equilibrium

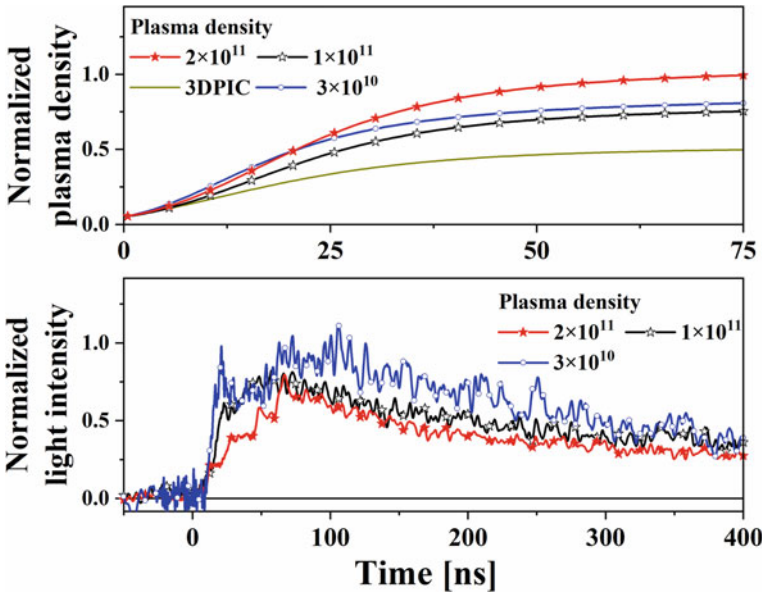

Fig. 8.31 **a** Calculated normalized plasma density $\eta = n_p(t)/n_p^0$ for different initial densities n_p^0. Neutral gas (Carbon) density $n_0 = 2 \times 10^{15}$ cm^{-3}. **b** Intensity of light registered by the side fiber and normalized by the initial plasma density n_p^0 (in arbitrary units) [13]

positions and to a large extent compensate the ion space charge in the waveguide's interior region, so that the electric field is concentrated mainly between the waveguide boundary and the almost quasi-neutral "plasma core." This is demonstrated in Fig. 8.32, where a normalized distribution of the electron density across the waveguide, obtained in the 3D PIC simulation, is depicted. The electron density is almost homogeneous up to ≈9 mm and drops sharply near the waveguide wall, so that uncompensated ions form a few millimeters thick "cladding," where the electric field is concentrated. The relative density of the ionization events is also shown in Fig. 8.32. The ionization events occur mostly on the waveguide axis and decrease gradually toward the periphery. This can explain the light intensity's experimentally observed radial profile (see Figs. 8.33 and 8.34), assuming that ionization and light emission occur in the same plasma region.

8.3.4 Experimental Results

The plasma luminosity profile during HPM propagation was observed by a fast-framing intensified camera (Stanford Computer Optics Inc. Model: 4Quick-E) (see Fig. 8.33). The microwave interaction with the plasma influences the light profile from originally almost homogeneous to strongly concentrated near the waveguide

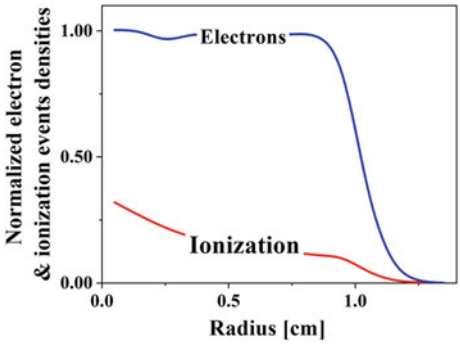

Fig. 8.32 Radial distributions of electrons and ionization events

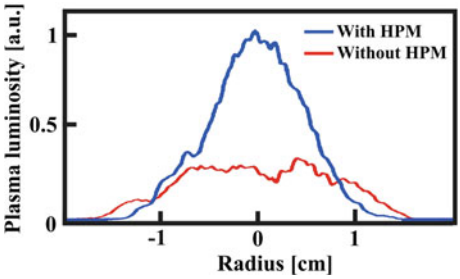

Fig. 8.33 Plasma luminosity distribution in $n_e \approx 5 \times 10^{10}$ cm^{-3} density plasma (red curve) in the absence of HPM and when the HPM pulse propagates through the plasma (blue curve). The light distribution in the presence of HPM was obtained at a time delay of ~2.4 ns relative to the moment the pulse enters the waveguide [13]

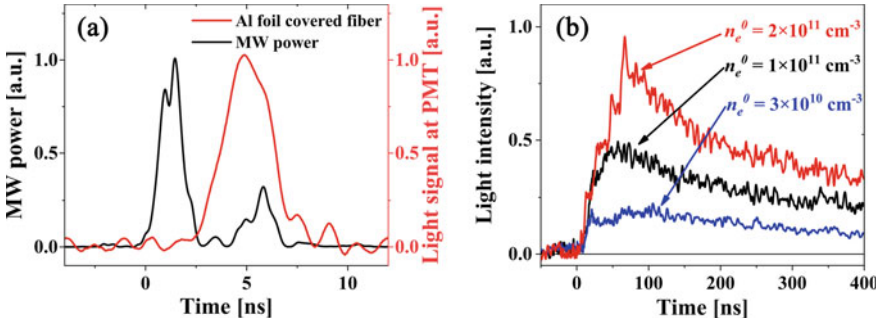

Fig. 8.34 **a** Typical waveform of the PMT attached to optical fiber covered by a 20 μm-thick Al foil (red) and the HPM power envelope (black) for a plasma density of $n_e \approx 5 \times 10^{10}$. **b** Light intensity registered by the side fiber for different densities of the plasma fill [13]

axis. This redistribution of the plasma luminosity cannot be associated with electron–ion collisions since for the plasma densities considered the collision frequency is lower than 10^6 s^{-1}.

The temporal behavior of the light emitted by electrons ejected from the waveguide in the radial direction, penetrating a 20 μm thick Al foil (electron energies ≥10 keV) covered optical fiber placed radially at a distance of 1.5 cm from the outer diameter of the waveguide (see Fig. 8.26), and the HPM pulse measured by coupler #1 for $n_e \approx 5 \times 10^{10}$ cm^{-3} are shown in Fig. 8.33a. One can see that the high-energy electrons appear at the tail of the HPM pulse as predicted in section "Fast Electron's Flux Through the Waveguide's Side Boundary". For 40 μm thick aluminum foil, no signal was detected. Therefore, the maximum energy of the electrons emitted over ~2 ns is not more than 25 keV. In vaccum, such high-energy electrons were not detected. This indicates that HPM induced background electron impact ionization of the remnant neutral gas is negligible.

Waveforms of light intensity obtained by an open faced side fiber for different densities of plasma are shown in Fig. 8.34b. The light intensity continues to grow during several tens of nanoseconds after the HPM pulse and decays slowly within hundreds of nanoseconds. Therefore, this long-time light emission is evidence for the strong perturbation of the plasma left by the HPM pulse in its wake in qualitative agreement with the model presented in section "Wake-Assisted Additional Ionization". When the HPM pulse propagated in vacuum, the same fiber detected a ~20 times smaller, ~3 ns long emitted light signal which as the result of the ionization of the background gas.

We also investigated the propagation of our second HPM source at 25.5 GHz HPM pulse through the plasma, and observe increased plasma light intensity. Typical plasma light patterns in the absence and presence of the HPM pulse are shown in Fig. 8.35 for different initial plasma densities. Increase in the density of the plasma leads to increase in light intensity. This is related to increase in the plasma electron energy and additional ionization/excitation of the background plasma ions and neutrals.

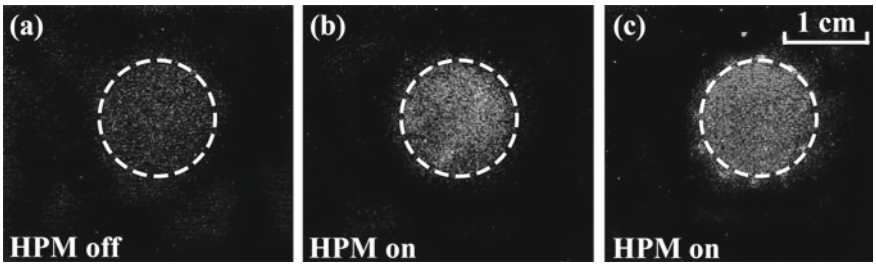

Fig. 8.35 Fast framing images taken by the 4QuikE fast framing (5 ns frame duration) intensified camera **a** in the absence of the HPM pulse and **b** when the 28.6 GHz HPM pulse through a plasma of density ~3×10^{12} cm^{-3} and **c** ~8×10^{12} cm^{-3}. The dashed line shows the inner boundary of the waveguide [5]

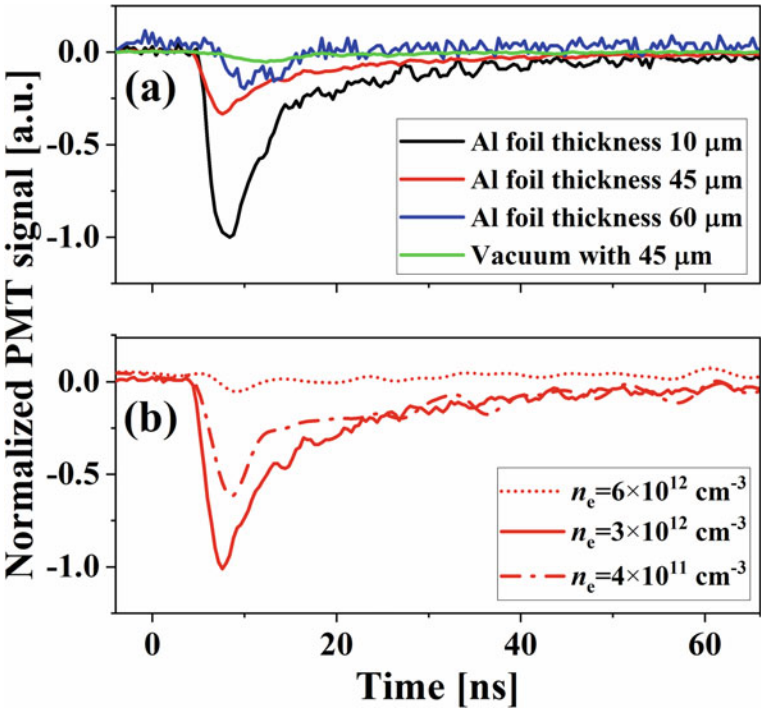

Fig. 8.36 Normalized **a** PMT signals of light emission induced by energetic electrons collected by the side fiber for various Al foil thicknesses and $n_e \approx 3 \cdot 10^{12}$ cm^{-3} and **b** for a fixed Al foil thickness of 45 μm for different plasmas densities [5]

For the 25.5 GHz source, energetic electrons in the radial direction have also been detected at different densities of the preliminary plasma (see Fig. 8.36). For $n_e \approx 3 \cdot 10^{12}$ cm^{-3}, energetic electrons have been registered up to 60 μm thickness Al foils which correspond to radially accelerated electrons of maximal energy $\leq$100 keV. Figure 8.36b shows that the appearance of such electrons is maximal for $n_e \approx 3 \cdot 10^{12}$ cm^{-3} density. As the density increase or decreases from this optimal value almost no signal was detected even when the thickness of Al foil was decreased to 10 μm.

For both frequencies of the microwave pulses, we found agreement with the theoretical analysis and the numerical simulations.

8.3.5 Frequency Shift and Pulse Compression

In the previous sections we investigated the effect of the HPM pulse on the plasma. The spatial distribution of the plasma electron density varies in time which in its turn, affects the pulse characteristics such as frequency, power, envelope shape etc.

which can be experimentally detected. Some of these effects will be considered in this section.

The ponderomotive force ejects electrons in the volume affected by the microwave pulse, while ions remain immobile. This displacement of the plasma electrons develops during the pulse. Therefore, the microwave pulse propagates in a time-dependent medium, which can affect the carrier frequency. The effect of the frequency shifts of a wave propagating through media characterized by nonstationary parameters is well-known and was studied both theoretically [40, 41] and experimentally [42–44].

In early studies, the temporal variation of the plasma density was associated with neutral gas ionization by the propagating powerful pulse [41] or laser beam [39, 42, 43]. Namely, an increase in the plasma density leads only to frequency up-shift [45]. During the development of the wake excitation in a waveguide filled with plasma, additional ionization can be neglected because of the short-duration of the pulse and the low preliminary density of the plasma. Thus, variations of the pulse spectrum may be associated with the evolution of the plasma density driven by the pulse itself. The plasma density perturbation follows the pulse along the waveguide. Interaction of the pulse with this co-propagating perturbation can be considered as a particular case of "front-induced transition" [46].

The wake excited by the microwave pulse contains consecutively placed regions of decreasing and increasing electron density regions. Depending on the position inside this wake, the local spectrum of the pulse is red- or blue-shifted. This specific property of the plasma, namely, its effect on the pulse can be used in wakefield "one-shot" diagnostics [47, 48] and pulse compression by group velocity dispersion [49]. It is important to note that filamentation and self-focusing, which are typical for the interaction of an electromagnetic pulse with transversally-unbound plasma [50, 51] are absent when the plasma is enclosed in a waveguide of radius comparable or less than the wavelength of the electromagnetic wave.

The dispersion equation of the TM mode of a cylindrical waveguide of radius R, filled with homogeneous plasma of density n_p, is given by

$$\omega^2 = c^2 k_z^2 + c^2 k_\perp^2 + \omega_p^2 \equiv c^2 k_z^2 + \Omega_0^2. \tag{8.3.11}$$

Note that Ω_0 is an eigenfrequency of the two-dimensional resonator formed by the waveguide cross section. Redistribution of the plasma density by the propagating pulse leads to the variation of this eigenfrequency in time and along the axial coordinate, z, so that $\Omega_0 = \Omega_0(t, z)$.

Variation of the frequency of the electromagnetic wave propagating through a medium with local dispersion characteristics defined by Eq. (8.3.11) with the time-dependent parameter $\Omega_0(t, z)$, is described by the following equation [41]:

$$\frac{\partial \omega^2}{\partial t} + v_g \frac{\partial \omega^2}{\partial z} = \frac{\partial \Omega_0^2}{\partial t}, \tag{8.3.12}$$

where v_g is the wave's group velocity. Equation (8.3.12) is valid when the characteristic temporal and spatial scales of the medium variation are large compared to the wave's period and wavelength, respectively.

Perturbation of the electron density n_e by the electromagnetic pulse propagates as a wake wave together with the pulse, i.e., with the group velocity v_g

$$n_e(t, z; r) = n_e\left(\frac{t}{v_g} - z; r\right). \tag{8.3.13}$$

This means that $\Omega_0(t, z) = \Omega_0(t/v_g - z)$ is constant along the characteristic of Eq. (8.3.12). Thus, Eq. (8.3.12) can be written in the form

$$\frac{d\omega^2(t)}{dt} = \frac{\partial\Omega_0}{\partial t}\Big|_{t_0} \tag{8.3.14}$$

Here, $\omega(t)$ is the local frequency of the pulse segment, which is injected into the system through the cross section $z = 0$ at the time t_0. Equation (8.3.14) means that the frequency shift, $\Delta\omega^2 = \omega^2(t) - \omega^2(t_0)$ grows linearly with the distance traveled by the pulse along the waveguide.

The change in the eigenfrequency of a cavity, $\delta\Omega_0$, due to a perturbation of the material (plasma) parameters within the cavity is described by the following expression (see e.g., Ref. [52]):

$$\frac{\Delta\Omega_0}{\Omega_0} \simeq -\frac{\int dV\left(\Delta\varepsilon\left|E_0^2\right| + \Delta\mu\left|H_0^2\right|\right)}{\int dV\left(\varepsilon\left|E_0^2\right| + \mu\left|H_0^2\right|\right)}, \tag{8.3.15}$$

where $\Delta\varepsilon$ and $\Delta\mu$ are the perturbations of the permittivity ε and the permeability μ, respectively, and $\overrightarrow{E}_0$ and $\overrightarrow{H}_0$ are the electric and magnetic fields of the eigenmode of the unperturbed cavity. The integration is performed throughout the volume of the cavity. For the case being considered, $\mu = 1$ and $\varepsilon = 1 - 4\pi e^2 n_e(r)/m\omega^2$, so that

$$\frac{\Delta\Omega_0}{\Omega_0} \simeq -\frac{\omega_{p0}^2}{\Omega_0}\frac{\int r dr\left[1 - \frac{n_e(r)}{n_0}\right]E_0^2(r)}{\int r dr\left[\left(1 - \omega_{p0}^2/\omega_0^2\right)E_0^2(r) + H_0^2(r)\right]}, \tag{8.3.16}$$

By using the 1D model described above, the electron density evolution during the microwave pulse propagation could be calculated and the frequency shift was calculated using Eqs. (8.3.14) and (8.3.16). Because the 1D model does not consider the pulse frequency variations, 3D LSP simulations were used to verify this approximation. The results of this comparison are shown in Fig. 8.37. It should be pointed out that the frequency's temporal variation, presented here, is similar to that obtained in Ref. [47], in spite of the difference in the geometry of the problems considered. One can see that there is a local frequency shift of the pulse due to the wake excitation, that is, the frequency of the leading part of the pulse is down-shifted, while its rear part is up-shifted. Consequently, the group velocity of the leading part is smaller than the group velocity of the rear part. This results in a decrease in the pulse's natural spread, eventually causing the pulse to compress. As an example, the pulse

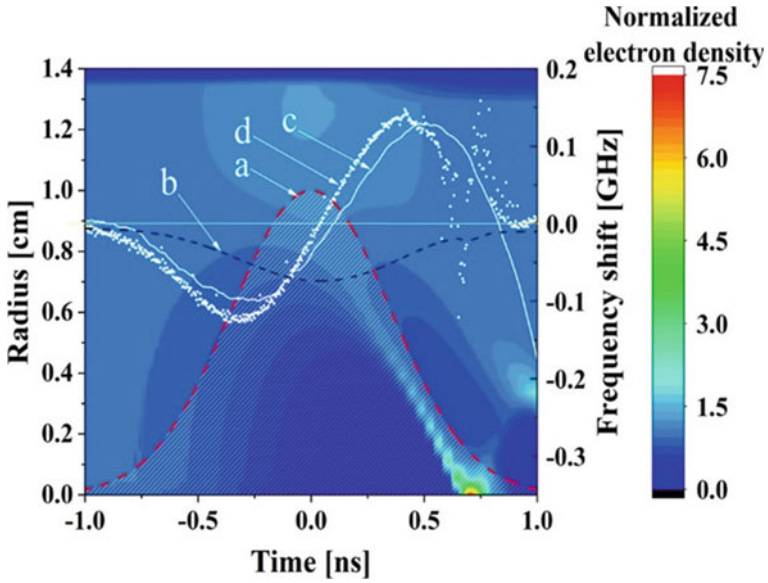

Fig. 8.37 Electron density perturbation and frequencies associated with the wake. **a** The envelope of the pulse power; **b** the eigen-frequency shift, $\Delta\Omega_0$, calculated using Eq. (8.3.16); **c** the local frequency shift $\Delta\omega$ of the pulse, calculated using Eq. (8.3.16); and **d** the local frequency shift $\Delta\omega$ calculated by wavelet analysis of the pulse's electric field component at a distance of 20 cm from the waveguide's input, using the LSP simulation results for an initial plasma density of 3×10^{10} cm^{-3} [13]

envelope's evolution while propagating in a waveguide in vacuum and in plasma are compared in Fig. 8.38a.

In the experiment, the downstream half of the flashboard plasma sources was turned off so that the plasma filled only the upstream half of the waveguide. The experimental results shown in Fig. 8.38b demonstrate that the HPM pulse compresses and its power increases by ~1.5.

8.3.6 Probing the Wake with an Electron Beam

To investigate the wake produced by ≤1.2 MW, 25.5 GHz, <0.6 ns high power microwave pulse when injected into a ~10^{10} cm^{-3} plasma-filled cylindrical waveguide we probed the perturbation along a line perpendicular to the waveguide axis by a thin low-current electron beam. This beam was produced by a specially designed gated electron gun with a point-like thermionic tungsten emitter attached to the outer walls of the experimental chamber so that the almost laminar electron beam with a cross-sectional diameter of ~1 mm FWHM and ≤60 μA amplitude, crossed two opposite slots of the slotted waveguide (see Fig. 8.39). This beam is then extracted

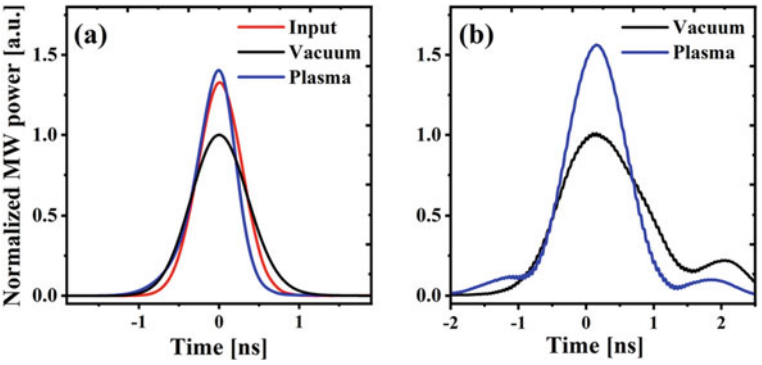

Fig. 8.38 **a** LSP pulse envelope at the waveguide input (red) ($z = 0$) and calculated at a distance of 60 cm in a 3×10^{10} cm^{-3} density plasma (blue) and in a vacuum (black); **b** experimentally observed pulse envelopes measured by coupler #2 for the vacuum (red) and when the plasma ($3 \cdot 10^{11}$ cm^{-3}) fills only the upstream half of the waveguide (black). All values are related to the normalized maximum of the power signal measured at the exit in the vacuum [12]

through a hole and collected on a fast plastic scintillator (Eljen Technology EJ-232Q, t_{decay} ~0.7 ns), placed at the exit from the chamber. The fluorescent light produced by the electrons in the scintillator is imaged at the 0.1 mm wide entrance slot of an Optronis SC-10 streak camera of sub-ns-temporal and sub-mm longitudinal resolution.

Using the LSP code, 3D PIC simulations were performed to evaluate the expected behavior of the probing electron beam. A pulse of 1.0 GW maximum power, 0.3 ns FWHM, 25.5 GHz in the TM_{01} mode is injected into a 1.5 cm diameter waveguide at $z = 0$ (the location of coupler #1 in Fig. 8.39). Between $z = 55$ cm and 80 cm a 10^{10} cm^{-3} density plasma fills the entire 6.5 cm radius flashboard chamber around

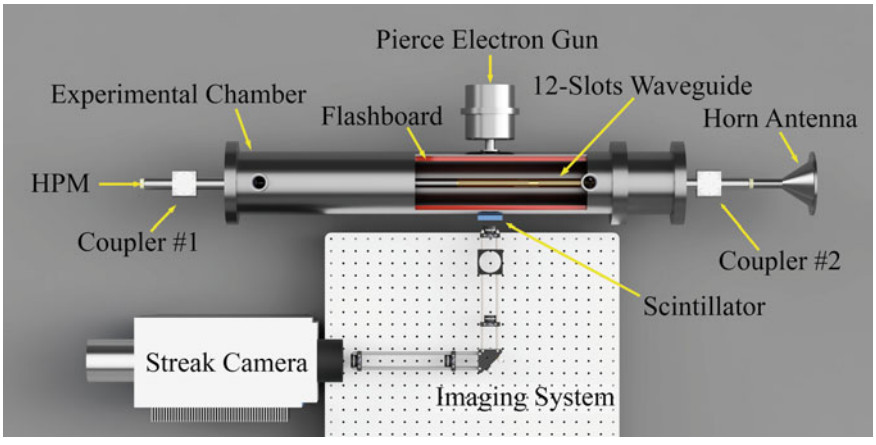

Fig. 8.39 The experimental setup

the slots and penetrates the waveguide overflowing 10 cm up- and downstream from the slotted region where it gradually decays to zero plasma density. During the short time considered (up to 15 ns) the ion motion is neglected. In Fig. 8.40 snapshots of the plasma density contours at times when the HPM pulse crosses the plasma are drawn. The white perpendicular line at $z = 67.5$ cm designates the unperturbed path of the probing electron beam which is injected at the outer radius $x = 6.25$ cm, crosses two opposite slots ($y = 0$) and is collected on a surface at $z = -6.5$ cm. The 10 keV injected beam had a Gaussian density distribution of ~1 mm (FWHM) and carried a current of 0.3 mA.

The plasma density modulation seen in Fig. 8.41 is in the form of a wake with a period of ~1 ns between the displayed minima and maxima in the density appearing along the axis. Between these maxima and minima there is approximately a factor of two in the density modulation accompanied by a wakefield of ~30 kV/cm which we expected to deflect the probing electron beam. Indeed, we found that the beam which before the arrival of the pulse flows along the line designated in Fig. 8.40, is strongly affected. In Fig. 8.41 the normalized total number of electrons of the probing beam along the scintillator [1 mm wide ($y = \pm 0.5$ mm, $x = -6.5$ cm $\pm$ 0.25 mm) and 2 mm long ($z = 67.5 \pm 1$ mm)] is drawn for the probing beam traversing the waveguide in vacuum and in plasma.

In both vacuum and plasma, no probe electrons reach the scintillator for ~1 ns (see Fig. 8.41 at ~7 ns). This is the direct result of the HPM pulse characterized on axis by a maximum electric field E_z = ~±500 kV/cm, and at radius ~5.5 mm by

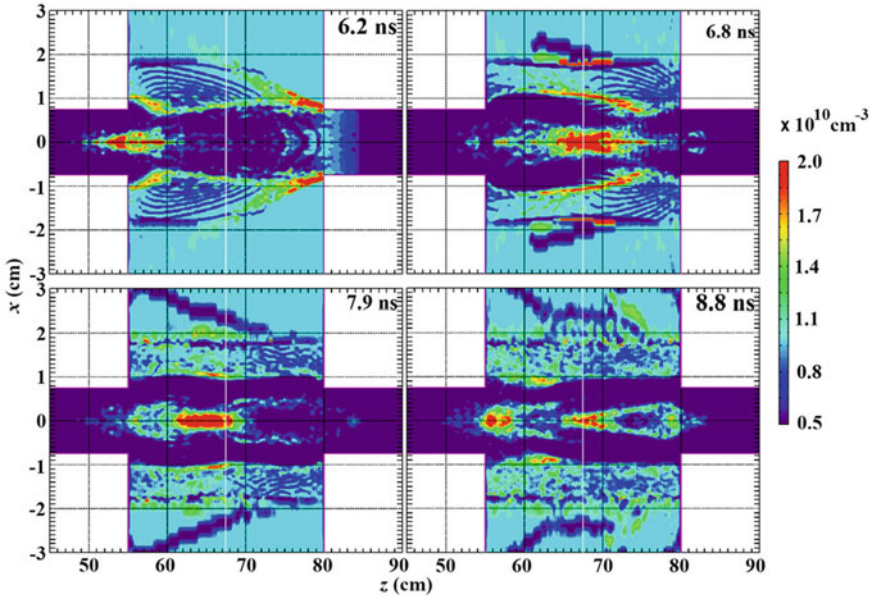

Fig. 8.40 Snapshots of plasma density contours in the $y = 0$ cross section at three consecutive times obtained in the LSP simulations

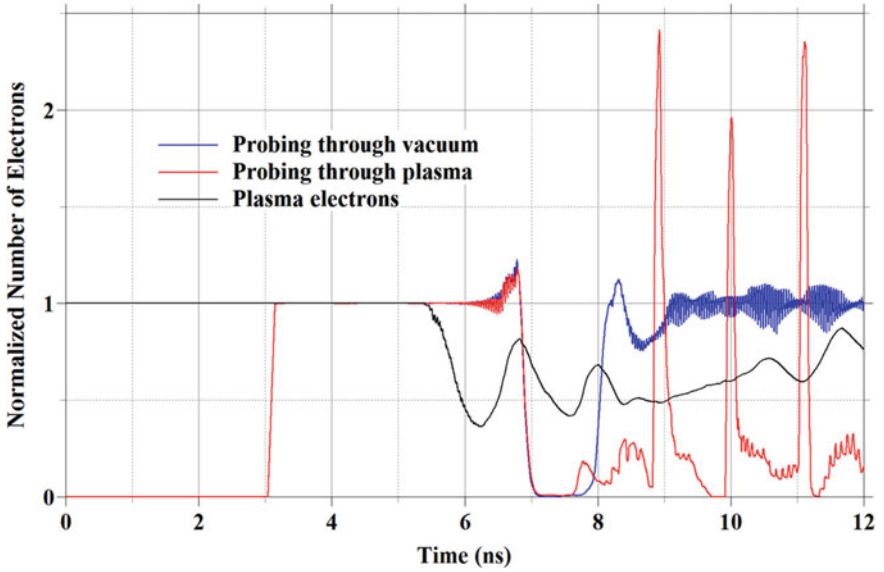

Fig. 8.41 The normalized total number of electrons of the probing beam along the scintillator in vacuum (blue) and in a 10^{10} cm^{-3} plasma (red). The total number of plasma electrons (black) along the unperturbed path of the probing beam inside the waveguide ($y = \pm$ 0.5 mm, $z = 67.5$ cm $\pm$ 1 mm, $x = \pm 6.25$ cm). Note that the probing beam arrives to the scintillator at ~3 ns whereas the plasma electrons have reached constant density long before the arrival of the pulse

E_r of the same order of magnitude, oscillating at 25.5 GHz. In vacuum one more small oscillation is observed at a later time (see blue curve in Fig. 8.41), the remnant effect of the HPM pulse's tail. Then almost no more perturbations are seen. For the plasma-filled waveguide, the minimum of the first trough in the density of the plasma seen in the black curve in Fig. 8.41 corresponds to the first snapshot in Fig. 8.40 at 6.2 ns. This is followed by the first maximum at ~6.8 ns (second snapshot in Fig. 8.3) and two more at 7.9 and 8.8 ns (see Fig. 8.40). This recurring plasma modulation continues for quite a long time. Not all are seen on the black curve because this curve represents the total number of electrons along the entire path of the probing beam in the waveguide. On the other hand, the scintillator picks up these modulations as sharp (~0.1 ns FWHM) recurring peaks (red curve in Fig. 8.41) in contrast to almost no perturbations in vacuum. Most of the beam electrons collected on the scintillator are concentrated in the $z = 67.5 \pm 1$ mm long region considered in Fig. 8.41, in agreement with the experiment (see Fig. 8.43).

The dynamics of the probing electron beam in the plasma-filled waveguide following the HPM pulse is more complex than that indicated by the appearance of the peaks seen in Fig. 8.41 (red curve) recurring at the same frequency as the frequency of the density modulation near the axis (Fig. 8.40). This is seen in the snapshots of the probing electron beam viewed in the $[z, x]$ plane including all beam electrons in the region y [−5 mm, 5 mm] at a few selected times. The region $x <$ −

6 cm corresponds to the location of the scintillator. The 6.8 ns frame of Fig. 8.42 corresponds to the appearance of the first trough in the red curve seen in Fig. 8.41. The probing beam was affected by the strong fields of the pulse to such an extent that it breaks which leaves a period of ~1 ns with no considerable signal on the scintillator. As it crosses the probing beam in vacuum, the microwave pulse causes beam breakup too. The rest of the snapshots are at later times long after the pulse has crossed the beam and the beam is affected only by the fields in the wake. The snapshot times correspond to the appearance times of the peaks in the red curve of Fig. 8.41. The wakefield, appearing at ~1 ns interval near the axis, kicks the probing beam so that it exits the waveguide following a trajectory typical to hose instability oscillating mostly in the z direction. Note that the spatial deflection of the beam becomes smaller as the wakefield becomes weaker in time.

The time delay between the beginning of the flashboard plasma formation and the HPM pulse generation, determines the plasma density encountered by the microwave pulse [8]. Due to the limited current of the probing electron beam, the ns-timescale streak image had insufficient luminescence to form a continuous beam pattern. Therefore, we overlaid multiple (4–6) streak images for the same experimental conditions resulting in the time dependent light bands concentrated over $\Delta z = \sim 2$ mm seen in Fig. 8.43a. These luminescence bands are summed over in z for each point in

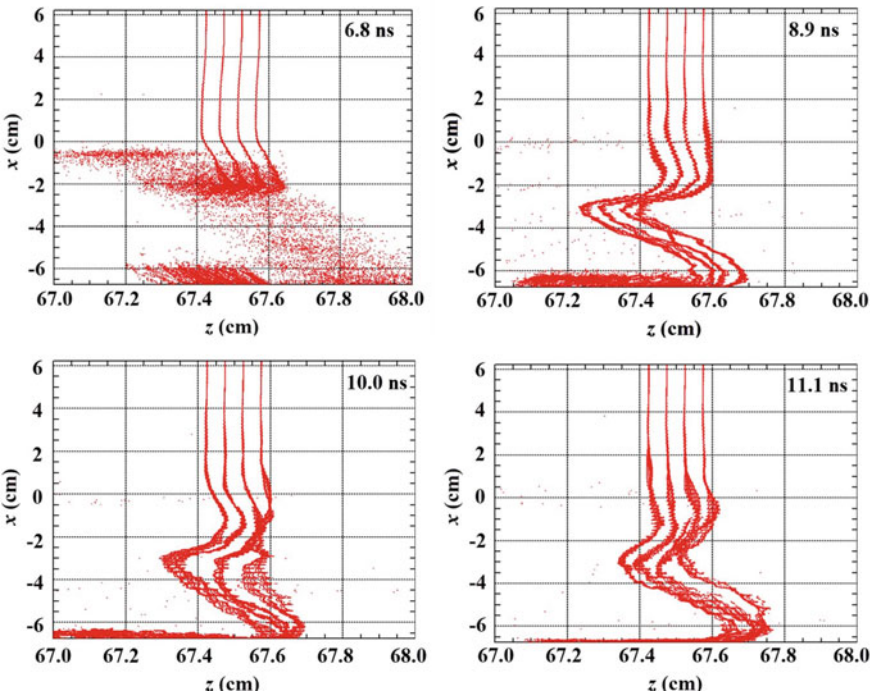

Fig. 8.42 Snapshots of the probing electron beam at increasing points in time

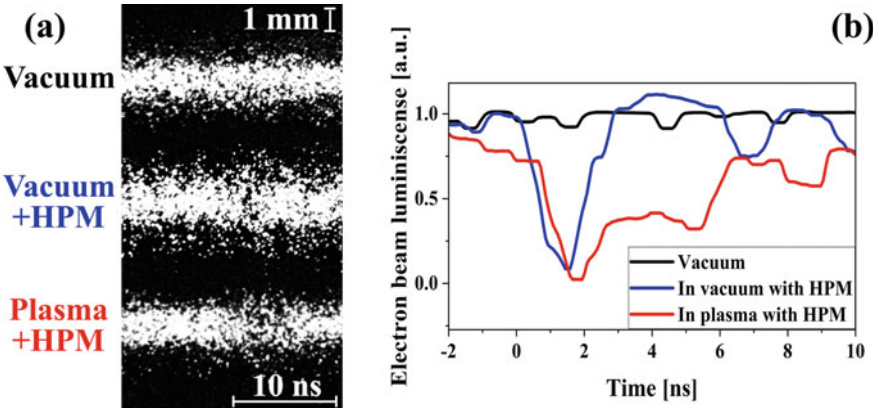

Fig. 8.43 **a** Overlaid multiple (4–6) streak images for the same experimental conditions resulting in the time dependent light bands concentrated over $\Delta z \cong 2$ mm obtained in vacuum without and with the HPM pulse and in plasma (~3×10^{10} cm^{-3}). **b** Time dependence of the averaged luminescence intensity seen in **a** in vacuum in the absence of the pulse (black) with the pulse (blue) and when the pulse traverses the plasma filled waveguide (red)

time, and the resulting in time dependent curves which were then averaged over time considering the resolution of the scintillator and the other parts of the optical imaging system to obtain the final results displayed in Fig. 8.43b.

The black curve in Fig. 8.43b is the result of the probing beam's almost constant trace on the scintillator. When the HPM pulse is switched on in vacuum it affects the probing beam (blue curve) in a similar manner as that observed in the simulation (blue curve in Fig. 8.41), that is, the microwave pulse causes the probing beam to break up and then return once it left the observation point. In the presence of ~3×10^{10} cm^{-3} density plasma, the HPM pulse makes the beam disappear at first just as in vacuum (red curve), followed by a period of ~3 ns with an almost constant light intensity of ~0.25 of the luminescence resulting from an unperturbed beam. The peaks seen in the simulation (red curve in Fig. 8.41) are not seen in the experiment because of the experimental time resolution and an average value is obtained only. Experiments with lower (~0.8 GW) power pulses or with high power pulses but at plasma densities >3×10^{10} cm^{-3}, result in a behavior similar to vacuum with HPM pulse which means that the resulting plasma perturbation is too small to cause the probing beam to deflect.

8.3.7 Nonlinear Absorption of HPM Pulses in a Plasma-Filled Waveguide

When the waveguide cutoff frequency, which depends on the plasma density, is close to the microwave frequency, the microwave pulse is completely absorbed and almost

no reflected or transmitted power is observed. Such absorption of the HPM pulse in a plasma-filled waveguide has not been observed or anticipated before because no appropriately high-power microwave sources were available.

Numerical Simulations

We used LSP to simulate the interaction of a 0.86 GW, 25.5 GHz and ~0.4 ns Gaussian pulse of total energy 0.19 J fed into a circular waveguide of the same diameter and length as in the experiment (15 mm and 80 cm respectively). Plasma fills the waveguide uniformly between the axial positions 55 and 80 cm with a 10 cm rising density upstream section and a 10 cm downstream decreasing density. The initially neutral plasma consists of uniformly distributed electrons and stationary ion macro-particles.

In Fig. 8.44a–c the time dependence of the HPM pulse is drawn at the input point to the waveguide (blue curves) and at the exit from the waveguide (red curves) for increasing plasma densities. In Fig. 8.44a at density 4×10^{12} cm^{-3} complete transmission is observed, at the slightly higher density of 5×10^{12} cm^{-3} (cutoff density) almost no signal is observed at both the input and output cross-sections which indicate complete power absorption in the plasma. At 8×10^{12} cm^{-3} the estimated critical density (Fig. 8.44c), complete reflection is observed at the input position, thus complete absorption occurs below the critical density. In Fig. 8.44d (complete transmission) when the HPM pulse encounters the plasma the electrons energy (W_e) increases by energy gained from the microwaves (W_{MW}). When the HPM pulse leaves the plasma, the electrons relax while returning energy to the HPM pulse. Finally, both the electron and field energy become nearly constant. In Fig. 8.44e (complete absorption) the electrons oscillate for a long time in the potential formed by the positive charge left in the waveguide as electrons leave the waveguide and collect on the walls. In Fig. 8.44f the plasma becomes reflective with some energy remaining in the plasma and energy exchange oscillations which relax fast.

In Fig. 8.45a, b simulation results are presented for a low maximum power MW pulse (8 W) which is to be compared to Fig. 8.44b, e respectively (0.86 GW). The transmitted and reflected waves are not negligible as in Fig. 8.44b and continue for longer times. The electrons energy and the MW pulse oscillate for a very small period of time and very little of the MW energy remains in the plasma after a long period of time compared to ~40% for the HPM pulse. Also, no electrons are lost on the walls. This shows that the electron dynamics for high and low power microwaves is completely different and the complete absorption phenomenon observed both experimentally (see below section "Experimental Results") and confirmed by simulations cannot be explained by the linear theory of wave absorption. As for wakefield situations during the propagation of the HPM pulse, the ponderomotive force moves part of the electrons to the walls of the waveguide resulting in an overall distributed positive charge potential in which the remaining electrons oscillate for long times.

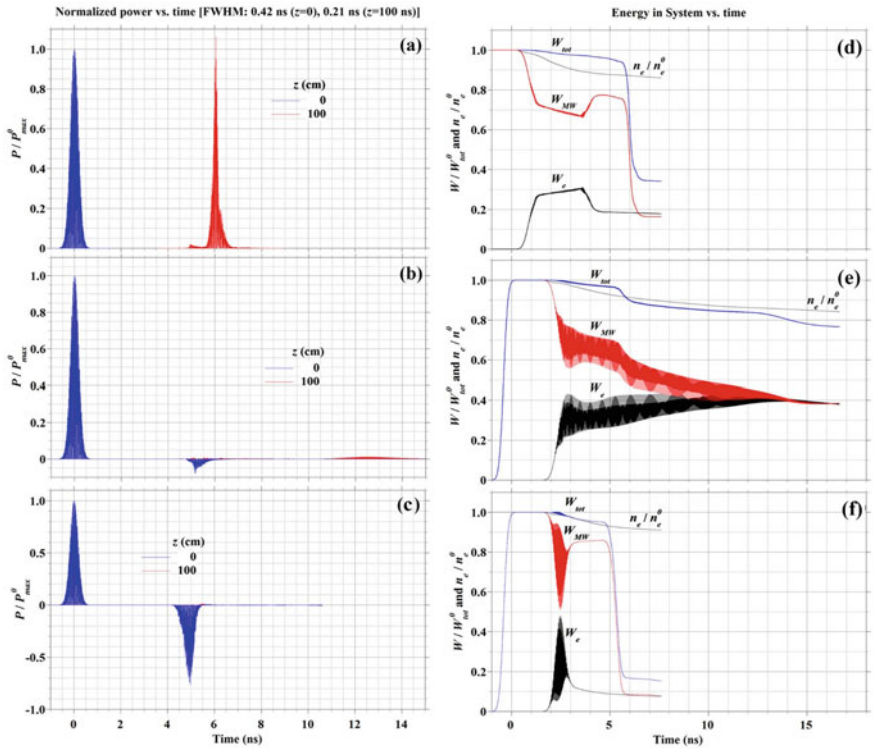

Fig. 8.44 **a–c** The time dependent normalized power signal, P, at $z = 0$ (blue) and $z = 100$ cm (red) normalized to the maximum power amplitude at $t = 0$, $P^0_{\max}$. **d–f** The total energy in the system, W_{tot}, (blue), the energy contained in the fields, W_{MW}, (red) and the kinetic energy of the electrons, W_e, (black) as function of time. All energies are normalized to the maximum energy input into the system by the HPM pulse, W^0_{tot}. The ratio between the number of electrons in the system, n_e, and the initial number of electrons, n^0_e, as function of time (grey) is drawn on the same scale. The plasma density is 4×10^{12} cm^{-3} in (**a**) and (**d**), 5×10^{12} cm^{-3} in (**b**) and (**e**), 8×10^{12} cm^{-3} in (**c**) and (**f**) [5]

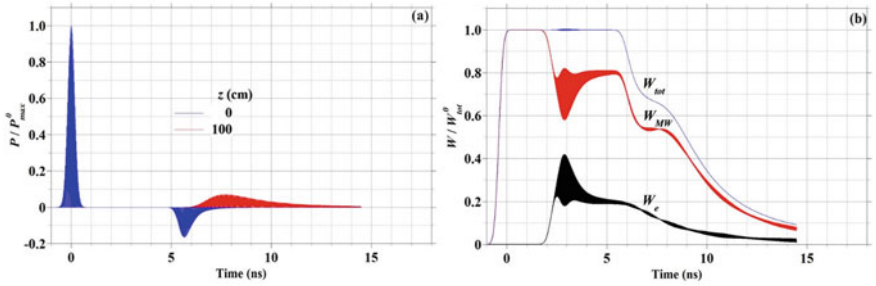

Fig. 8.45 Same as Fig. 8.38 for the plasma density 5×10^{12} cm^{-3} but for a very low maximum power MW pulse (8 W) [5]

Experimental Results

In Fig. 8.46, one can see the incident, transmitted, and reflected power signal of the HPM pulses registered by the two couplers in vacuum at the entrance and output of the waveguide and at various plasma densities. In vacuum (see Fig. 8.46a), the maximum transmitted power decreased (~25%), while the pulse width increased. At the same time, almost no energy is lost. For a plasma density of $(3 \pm 1) \times 10^{12}$ cm^{-3}, there are no reflections, and the transmitted power signal is lower and wider (Fig. 8.46b). At $(5 \pm 1) \times 10^{12}$ cm^{-3} (Fig. 8.46c), we observe very small reflection and negligible transmission, and these small amplitude traces are smeared in time. At the slightly higher plasma density of $(8 \pm 1) \times 10^{12}$ cm^{-3} (Fig. 8.46d), only the reflected pulse appears. All the plasma densities considered are close to critical (8×10^{13} cm^{-3}). Even at the plasma density of 10^{13} cm^{-3}, the maximum of the reflected HPM power is less than 50% of the incident power.

We define transmission and reflection coefficients as the ratio of the energy contained in the transmitted and reflected signals, respectively, normalized to the energy contained in the HPM pulse incident at the coupler located at the waveguide entrance. The dependence of these experimentally measured transmission and reflection coefficients on plasma density is shown in Fig. 8.47. One can see that at the plasma density of $(5 \pm 0.5) \times 10^{12}$ cm^{-3}, the transmitted and reflected coefficients are both very low. This indicates almost complete absorption of the HPM pulse by the plasma. With increasing plasma density, the reflection coefficient increases, but a rather strong absorption is still evident. These results are in good agreement with 3D numerical simulations and theoretical modeling.

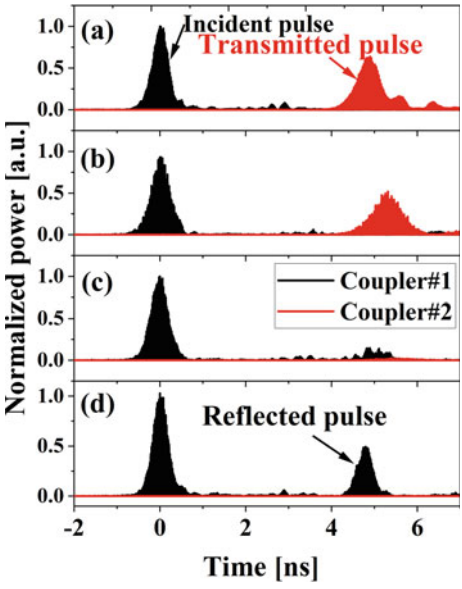

Fig. 8.46 The incident, transmitted, and reflected HPM pulse registered in **a** vacuum and at **b** $(3 \pm 1) \times 10^{12}$ cm^{-3}, **c** $(5 \pm 1) \times 10^{12}$ cm^{-3}, and **d** $(8 \pm 1) \times 10^{12}$ cm^{-3} plasma densities [5]

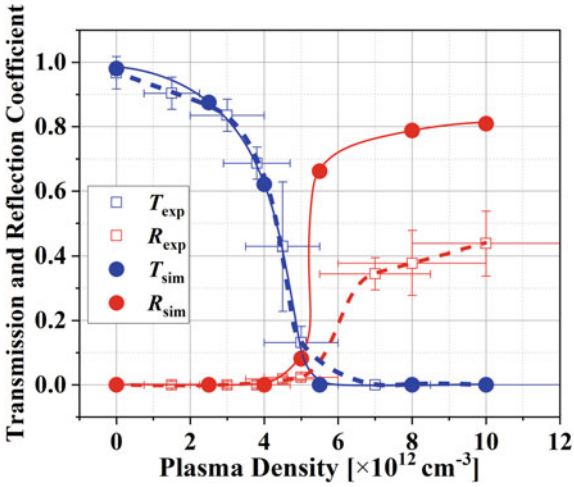

Fig. 8.47 Transmission (blue) and reflection (red) coefficients for HPM pulses at various plasma densities [5]

8.4 Summary

This review describes novel non-linear phenomena accompanying the propagation of short ($\leq$1 ns) pulses of high-power (hundreds of MW, GW) high-frequency (10–30 GHz) electromagnetic radiation through a neutral gas and plasma, in open space and in waveguides. These effects were either new or not observed experimentally before. Ionization-induced wave beam self-channeling in a neutral gas was theoretically predicted in Ref. [24] in 1987, but only our experimental conditions allowed this phenomenon to be observed in the laboratory. A detailed theoretical analysis and numerical simulation made it possible to explain the observed accompanying results such as the change in the pulse shape, the appearance of side scattering and the generation of high energy electrons.

Of particular interest are studies of the phenomena accompanying the propagation of a pulse in a plasma filled waveguide. Experimental studies applying such ultrashort and extremely high intensity electromagnetic pulses produced by our unique source of electromagnetic radiation, a super-radiant backward wave oscillator, have not been carried out before. The source injects HPM pulse directly into the waveguide. This leads to a number of phenomena, not characteristic to free plasma. Among these are the following:

1. Depending on the ratio between the cutoff frequencies of the waveguide and the carrier frequency of the pulse, the perturbation of the electron density is maximum either on the axis or on the periphery of the waveguide.
2. A significant part of the plasma electrons is ejected toward the waveguide wall and absorbed by it, leaving an uncompensated positive charge in the waveguide.
3. The release of high-energy electrons to the walls accompanies the propagation of the pulse and is one of the mechanisms of its energy dissipation. For some values

of the plasma and pulse parameters, the entire pulse energy can completely be absorbed.
4. Microwave pulse compression and frequency shift accompany the formation of the wake field obtained for a certain range of the plasma parameters.

The detection of these effects required creating sophisticated experimental equipment and the use of sophisticated numerical diagnostic methods. These methods are described in detail together with analytical and numerical studies.

References

1. N.S. Ginzburg, N.Y. Novozhilova, I.V. Zotova, A.S. Sergeev, N.Y. Peskov, A.D. Phelps, S.M. Wiggins, A.W. Cross, K. Ronald, W. He, V.G. Shpak, M.I. Yalandin, S.A. Shunailov, M.R. Ulmaskulov, V.P. Tarakanov, Generation of powerful subnanosecond microwave pulses by intense electron bunches moving in a periodic backward wave structure in the superradiative regime. Phys. Rev. E. Stat. Phys. Plasmas. Fluids. Relat. Interdiscip. Topics **60**, 3297 (1999)
2. A.A. Eltchaninov, S.D. Korovin, V.V. Rostov, I.V. Pegel, G.A. Mesyats, S.N. Rukin, V.G. Shpak, M.I. Yalandin, N.S. Ginzburg, Production of short microwave pulses with a peak power exceeding the driving electron beam power. Laser Part. Beams **21**, 187 (2003)
3. Y.P. Bliokh, J.G. Leopold, G. Shafir, A. Shlapakovski, Y.E. Krasik, Wakefield in a waveguide. Phys. Plasmas **24**, 063112 (2017)
4. G. Shafir, A. Shlapakovski, M. Siman-Tov, Y. Bliokh, J.G. Leopold, S. Gleizer, R. Gad, V.V. Rostov, Y.E. Krasik, High power microwave source for a plasma wakefield experiment. J. Appl. Phys. **121**, 033301 (2017)
5. Y. Cao, J.G. Leopold, Y.P. Bliokh, G. Leibovitch, Y.E. Krasik, Nonlinear absorption of high-power microwave pulses in a plasma filled waveguide. Phys. Plasmas **28**, 062307 (2021)
6. G. Shafir, D. Zolotukhin, V. Godyak, A. Shlapakovski, S. Gleizer, Y. Slutsker, R. Gad, V. Bernshtam, Y. Ralchenko, Y.E. Krasik, Characterization of inductively coupled plasma generated by a quadruple antenna. Plasma Sour. Sci. Technol. **26** (2017)
7. G. Shafir, Y. Cao, Y. Bliokh, J.G. Leopold, D. Levko, V. Rostov, R. Gad, A. Fisher, V. Bernshtam, Y.E. Krasik, The interaction of intense, ultra-short microwave beams with the plasma generated by gas ionization. Phys. Plasmas **25**, 032308 (2018)
8. Y. Cao, J.G. Leopold, Y.P. Bliokh, Y.E. Krasik, Self-channeling of a powerful microwave beam in a preliminarily formed plasma. Phys. Plasmas **25**, 103101 (2018)
9. G. Shafir, Y.E. Krasik, Y.P. Bliokh, D. Levko, Y. Cao, J.G. Leopold, R. Gad, V. Bernshtam, A. Fisher, Ionization-induced self-channeling of an ultrahigh-power subnanosecond microwave beam in a neutral gas. Phys. Rev. Lett. **120**, 135003 (2018)
10. Y. Krasik, J. Leopold, G. Shafir, Y. Cao, Y. Bliokh, V. Rostov, V. Godyak, M. Siman-Tov, R. Gad, A. Fisher, V. Bernshtam, S. Gleizer, D. Zolotukhin, Y. Slutsker, Experiments designed to study the non-linear transition of high-power microwaves through plasmas and gases. Plasma **2**, 51 (2019)
11. Y. Cao, Y. Bliokh, J.G. Leopold, V. Rostov, Y. Slutsker, Y.E. Krasik, Wakefield excitation by a powerful sub-nanosecond 28.6 GHz microwave pulse propagating in a plasma filled waveguide. Phys. Plasmas **26**, 023102 (2019)
12. Y. Cao, J.G. Leopold, Y.P. Bliokh, A. Li, G. Shafir, A. Fisher, G. Leibovitch, V.V. Rostov, Y.E. Krasik, The interaction of a high-power sub-nanosecond microwave pulse with plasma. IEEE Trans. Plasma Sci. **48**, 792 (2020)
13. Y. Cao, Y.P. Bliokh, J.G. Leopold, A. Li, G. Leibovitch, Y.E. Krasik, Wake excitation by a powerful microwave pulse and its evolution in a plasma-filled waveguide. Phys. Plasmas **27**, 053103 (2020)

14. J. Benford, J.A. Swegle, E. Schamiloglu, *High Power Microwaves*, 3rd edn. (CRC Press, 2015)
15. N.S. Ginzburg, I.V. Zotova, A.W. Cross, A.D.R. Phelps, M.I. Yalandin, V.V. Rostov, Generation, amplification, and nonlinear self-compression of powerful superradiance pulses. IEEE Trans. Plasma Sci. **41**, 646 (2013)
16. A.A. El'chaninov, S.D. Korovin, V.V Rostov, I.V. Pegel', G.A. Mesyats, M.I. Yalandin, N.S. Ginzburg, Cherenkov superradiance with a peak power higher than electron flow power. J. Exp. Theor. Phys. Lett. **77**, 266 (2003)
17. N.S. Ginzburg, I.V. Zotova, I.V. Pegel, V.V. Rostov, V.G. Shpak, M.I. Yalandin, Generation of high-power ultrashort electromagnetic pulses on the basis of effects of superradiance of electron bunches. Radiophys. Quantum Electron. **50**, 762 (2007)
18. B. Goplen, L. Ludeking, D. Smith, G. Warren, User-configurable MAGIC for electromagnetic PIC calculations. Comput. Phys. Commun. **87**, 54 (1995)
19. P. Sprangle, C.-M. Tang, E. Esarey, Relativistic self-focusing of short-pulse radiation beams in plasmas. IEEE Trans. Plasma Sci. **15**, 145 (1987)
20. F.W. Perkins, E.J. Valeo, Thermal self-focusing of electromagnetic waves in plasmas. Phys. Rev. Lett. **32**, 1234 (1974)
21. Y. Tamaki, J. Itatani, Y. Nagata, M. Obara, K. Midorikawa, Highly efficient, phase-matched high-harmonic generation by a self-guided laser beam. Phys. Rev. Lett. **82**, 1422 (1999)
22. G.-Z. Sun, E. Ott, Y.C. Lee, P. Guzdar, Self-focusing of short intense pulses in plasmas. Phys. Fluids **30**, 526 (1987)
23. D.J. Spence, A. Butler, S.M. Hooker, Gas-filled capillary discharge waveguides. J. Opt. Soc. Am. B **20**, 138 (2003)
24. Y.L. Bogomolov, S.F. Lirin, V.E. Semenov, A.M. Sergeev, Ionization self-channeling of extremely intense electromagnetic-waves in a plasma. JETP Lett. **45**(11), 680 (1987)
25. A.G. Litvak, Nonlinear dynamics of a freely localized gas discharge in microwave beams, in *The International Workshop on Strong Microwave in Plasmas*, ed. by A.G. Litvak (Institute of Applied Physics, USSR Academy of Science, Nishny Novgorod, 1991), pp. 267–286
26. Y. Ralchenko, R.K. Janev, T. Kato, D.V. Fursa, I. Bray, F.J. de Heer, Electron-impact excitation and ionization cross sections for ground state and excited helium atoms. At. Data Nucl. Data Tables **94**, 603 (2008)
27. D.R. Welch, D.V. Rose, B.V. Oliver, R.E. Clark, Simulation techniques for heavy ion fusion chamber transport. Nucl. Instrum. Methods Phys. Res. Sect. A Accel. Spectrometers, Detect. Assoc. Equip. **464**, 134 (2001)
28. C. Thoma, T.P. Hughes, N.L. Bruner, T.C. Genoni, D.R. Welch, R.E. Clark, Monte Carlo versus bulk conductivity modeling of RF breakdown of helium. IEEE Trans. Plasma Sci. **34**, 910 (2006)
29. D.V. Rose, D.R. Welch, R.E. Clark, C. Thoma, W.R. Zimmerman, N. Bruner, P.K. Rambo, B.W. Atherton, Towards a fully kinetic 3D electromagnetic particle-in-cell model of streamer formation and dynamics in high-pressure electronegative gases. Phys. Plasmas **18**, 93501 (2011)
30. T. Tajima, J.M. Dawson, Laser electron accelerator. Phys. Rev. Lett. **43**, 267 (1979)
31. E. Esarey, C.B. Schroeder, W.P. Leemans, Physics of laser-driven plasma-based electron accelerators. Rev. Mod. Phys. **81**, 1229 (2009)
32. V. Malka, Laser plasma accelerators. Phys. Plasmas **19**, 055501 (2012)
33. W.P. Leemans, B. Nagler, A.J. Gonsalves, C. Tóth, K. Nakamura, C.G.R. Geddes, E. Esarey, C.B. Schroeder, S.M. Hooker, GeV electron beams from a centimetre-scale accelerator. Nat. Phys. **2**, 696 (2006)
34. H.K. Malik, Analytical calculations of wake field generated by microwave pulses in a plasma filled waveguide for electron acceleration. J. Appl. Phys. **104**, 053308 (2008)
35. S.K. Tomar, H.K. Malik, Density modification by two superposing TE10modes in a plasma filled rectangular waveguide. Phys. Plasmas **20** (2013)
36. Y.E. Krasik, A. Weingarten, Energetic electron and ion beam generation in plasma opening switches. IEEE Trans. Plasma Sci. **26**, 208 (1998)
37. L.M. Earley, W.P. Ballard, C.B. Wharton, New directional couplers for multimode circujlar waveguides applied to intense pulsed microwave systems. IEEE Trans. Nucl. Sci. **32**, 2921 (1985)

38. M.J. Berger, J.S. Coursey, M.A. Zucker, J. Chang, Stopping-power & range tables for electrons, protons, and helium ions. https://doi.org/10.18434/T4NC7P
39. D.R. Welch, D.V. Rose, M.E. Cuneo, R.B. Campbell, T.A. Mehlhorn, Integrated simulation of the generation and transport of proton beams from laser-target interaction. Phys. Plasmas **13**, 063105 (2006)
40. E. Yablonovitch, Self-phase modulation and short-pulse generation from laser-breakdown plasmas. Phys. Rev. A **10**, 1888 (1974)
41. V.B. Gildenburg, V.A. Krupnov, V.E. Semonov, Frequency self-conversion and reflectionless propagation of the high-frequency electromagnetic pulse at the breakdown conditions. Sov. Tech. Phys. Lett **14** (1988)
42. S.P. Kuo, Frequency up-conversion of microwave pulse in a rapidly growing plasma. Phys. Rev. Lett. **65**, 1000 (1990)
43. E. Esarey, G. Joyce, P. Sprangle, Frequency up-shifting of laser pulses by copropagating ionization fronts. Phys. Rev. A **44**, 3908 (1991)
44. A. Giulietti, A. André, S. Dobosz Dufrénoy, D. Giulietti, T. Hosokai, P. Koester, H. Kotaki, L. Labate, T. Levato, R. Nuter, N.C. Pathak, P. Monot, L. A. Gizzi, Space- and time-resolved observation of extreme laser frequency upshifting during ultrafast-ionization. Phys. Plasmas **20**, 082307 (2013)
45. J.K. Koga, N. Naumova, M. Kando, L.N. Tsintsadze, K. Nakajima, S.V. Bulanov, H. Dewa, H. Kotaki, T. Tajima, Fixed blueshift of high intensity short pulse lasers propagating in gas chambers. Phys. Plasmas **7**, 5223 (2000)
46. M.A. Gaafar, T. Baba, M. Eich, A.Y. Petrov, Front-induced transitions. Nat. Photonics **13**, 737 (2019)
47. J.M. Dias, L. Oliveira e Silva, J.T. Mendonça, Photon acceleration versus frequency-domain interferometry for laser Wakefield diagnostics. Phys. Rev. Spec. Top.—Accel. Beams **1**, 31301 (1998)
48. C.D. Murphy, R. Trines, J. Vieira, A.J.W. Reitsma, R. Bingham, J.L. Collier, E.J. Divall, P.S. Foster, C.J. Hooker, A.J. Langley, P.A. Norreys, R.A. Fonseca, F. Fiuza, L.O. Silva, J.T. Mendonça, W.B. Mori, J.G. Gallacher, R. Viskup, D.A. Jaroszynski, S.P.D. Mangles, A.G.R. Thomas, K. Krushelnick, Z. Najmudin, Evidence of photon acceleration by laser wake fields. Phys. Plasmas **13**, 33108 (2006)
49. W.P. Leemans, C.W. Siders, E. Esarey, N.E. Andreev, G. Shvets, W.B. Mori, Plasma guiding and wakefield generation for second-generation experiments. IEEE Trans. Plasma Sci. **24**, 331 (1996)
50. C. Ren, B.J. Duda, R.G. Hemker, W.B. Mori, T. Katsouleas, T.M. Antonsen, P. Mora, Compressing and focusing a short laser pulse by a thin plasma lens. Phys. Rev. E **63**, 026411 (2001)
51. O. Shorokhov, A. Pukhov, I. Kostyukov, Self-compression of laser pulses in plasma. Phys. Rev. Lett. **91**, 265002 (2003)
52. R.F. Harrington, *Time-Harmonic Electromagnetic Fields* (Wiley-IEEE Press, 2001)